Title:

Regional and LTP-Dependent Variation of Synaptic Information Storage Capacity in Rat Hippocampus

Authors:

Mohammad Samavat[1,2*]**, Thomas M. Bartol**[2]**, Cailey Bromer**[2]**, Jared B. Bowden**[4]**, Dusten D. Hubbard**[4]**, Dakota C. Hanka**[4]**, Masaaki Kuwajima**[4]**, John M. Mendenhall**[4]**, Patrick H. Parker**[4]**, Wickliffe C. Abraham**[6*]**, Kristen M. Harris**[4,5*]**, Terrence J. Sejnowski**[2,3*]

Affiliations:

1-Department of Electrical and Computer Engineering, Jacobs School of Engineering, UC San Diego; 2-Computational Neurobiology Laboratory, The Salk Institute for Biological Sciences, La Jolla, CA 92037; 3-Division of Biological Sciences, University of California, San Diego, La Jolla, CA 92093; 4-Center for Learning and Memory, The University of Texas at Austin, Austin, TX 78712; 5-Department of Neuroscience, The University of Texas at Austin, Austin, TX 78712; 6-Department of Psychology, University of Otago, 9054 Dunedin, New Zealand

*For correspondence:
Email:
terry@salk.edu (TJS);
kharris@utexas.edu (KMH);
cliff.abraham@otago.ac.nz (WCA);
msamavat@ucsd.edu (MS)

Abstract
Synapses from the same axon onto the same dendrite have a common history of coactivation and have similar spine head volumes, suggesting that synapse function precisely modulates structure. We have applied Shannon information theory to obtain a new analysis of synaptic information storage capacity (SISC) using non-overlapping dimensions of dendritic spine head volumes as a measure of synaptic weights with distinct states. Spine head volumes in the stratum radiatum of hippocampal area CA1 occupied 24 distinct states (4.1 bits). In contrast, spine head volumes in the middle molecular layer of control dentate gyrus occupied only 5 distinct states (2 bits). Thus, synapses in different hippocampal regions had different synaptic information storage capacities. Moreover, these were not fixed properties but increased during long-term potentiation, such that by 30 min following induction, spine head volumes in the middle molecular layer increased to occupy 10 distinct states (3 bits), and this increase lasted for at least 2 hours. Measurement of the Kullback-Liebler divergence revealed that synaptic states evolved closer to storing the maximum amount of information during long-term potentiation. These results show that our new SISC analysis provides an improved and reliable estimate of information storage capacity of synapses. SISC revealed that the Shannon information after long-term potentiation is nearly maximized for the number of distinguishable states.

Introduction

In the late 19th century, Santiago Ramón y Cajal proposed that memories are stored at synapses and not through the generation of new neurons (**Ramón y Cajal, 1894**). Since then, there has been an extensive search for synaptic mechanisms responsible for learning and memory. In particular, long-term potentiation (LTP) has become a standard model for investigating cellular, synaptic, and molecular mechanisms of learning and memory. Numerous structural consequences have been shown to accompany LTP. For example, the density of docked vesicles at the presynaptic active zone area is increased and may explain the enhanced release probability (**Jung et al., 2021**). Dendritic spines and the area of the postsynaptic density (PSD) enlarge at the expense of new spine outgrowth in the mature hippocampus (**Bourne and Harris, 2011; Bell et al., 2014; Harris, 2020**). Although synaptic plasticity is well-established as an experience-dependent mechanism for modifying these and other synaptic features, the precision of this mechanism is unknown. The existence of both intrinsic and extrinsic origins of variability and dysfunction of structural modulation (**Kasai et al., 2021**) motivates further exploration of the potential precision with which synaptic strengths can be adjusted. From an information theory point of view, there can be no information stored without precision – the more precise synaptic plasticity is, the more distinguishable synaptic states are possible and the greater amount of information that can be stored at the synapses in a particular neural circuit.

Several studies have shown that synaptic strength is highly correlated with dendritic spine head volume (**Harvey and Svoboda, 2007; Matsuzaki et al., 2004; Harris, 2020, reviewed papers in Yang and Lui, 2022**). In previous studies (**Bartol et al., 2015, Bromer et al., 2018**), signal detection theory was used to calculate the number of discriminable synaptic strengths with an assumed signal-to-noise ratio across the range of spine head volumes. Pairs of dendritic spines on the same dendrite that receive input from the same axon (SDSA pairs) occur naturally in the brain and are expected to have experienced the same activation histories (**Harris and Sorra, 1998; Kumar et al., 2020**). Hence, synaptic precision can be estimated by measuring the difference between the spine head volumes of SDSA pairs. Outcomes from analyses of CA1 pyramidal cell dendrites revealed a remarkably high precision with more than 4 bits of information stored in spine head volumes (**Bartol et al., 2015**) and 2-3 bits in dentate gyrus (**Bromer et al., 2018**). This highly significant difference likely reflects the known differences between area CA1 and dentate gyrus in activation histories and functions in memory formation (**Snyder, et al., 2001; Saxe, et al., 2006; Krueppel, et al., 2011; Lopez-Rojas, et al., 2016**).

Here we used information theory to develop a new method using reconstructed dendrites that quantifies empirically the SISC – the number of bits of Shannon information stored per synapse. In the new method, the precision analysis is based on the coefficient of variation (CV) of SDSA pairs, the same starting point as in Bartol et al. (2015). The new method, however, performs non-overlapping cluster analysis (Algorithm 2) to obtain the number of distinguishable categories (N_C) of spine head volumes using the precision level estimated from the CV. The maximum number of bits is calculated as the $\log_2(N_C)$ which sets an upper bound for SISC. The Shannon information per synapse was calculated from the frequency of spine head volumes in the distinguishable categories where each category is considered a different message. We then explored the information coding efficiency at synapses by measuring Kullback-Leibler (KL) divergence between the spine head volume distributions measured in the control and LTP conditions as compared with a uniform distribution.

Comparison of the new SISC measurements with the previous results demonstrates that the new method is more robust to outliers and, importantly, can reveal gaps and variation in the shape of the distribution. In contrast, with signal detection theory gaps were filled in with Gaussians in the absence of any data. SISC was applied to synapses in control hippocampal area CA1 that was perfusion-fixed *in vivo*, and in the dentate gyrus (Dentate Gyrus) perfusion-fixed at 30 minutes and 2 hours after the induction of unilateral LTP *in vivo*. The results reveal robust differences between the brain regions and across conditions of synaptic plasticity.

Results

### Induction of LTP in the Dentate Gyrus

We analyzed 3D reconstruction from serial section electron microscopy (3DEM) datasets containing perforant path synapses in the middle molecular layer (MML) of the Dentate Gyrus for inputs arising from the medial entorhinal cortex. Data were collected from the stimulated hippocampus of two rats at 30 min and two rats at 2 hours post-induction of LTP, with the hippocampus in the opposite hemisphere serving as the control. All experiments were conducted in the middle of the animals' waking (dark) period to control for variation due to the circadian cycle (*Bowden et al., 2012*). Analysis of the 30 min control and LTP datasets using our previous signal detection method (*Bartol et al., 2015*) was published in *Bromer et al. (2018*).

We used the previously described methods to induce LTP in the MML of freely moving rats (*Bowden et al., 2012*). Briefly, stimulating electrodes were surgically implanted in both the medial and lateral perforant paths of the LTP hemisphere, and an additional stimulating electrode was implanted in the medial path of the control hemisphere. Field potential recordings were made using electrodes placed bilaterally in the dentate hilus. Animals were allowed to recover for two weeks prior to producing LTP or control stimulation during the animals' dark (waking) part of the circadian cycle. LTP was induced by 50 trains of unilateral delta-burst stimulation to the medial path electrode and then recorded for either 30 min or 2 hr, timed from the beginning of the delta-burst stimulation. Relative to the two control hemispheres, the LTP hemispheres showed an average of 41% potentiation in the MML for the 30 min experiment (Fig. 1A, B). In the 2 hr experiment, there was an average of 37% LTP for the two animals (*Fig. 1*C).

Serial electron micrographs and 3D reconstructions were prepared from the control (*Fig. 1*D) and 30 min LTP (*Fig. 1*E) hemispheres of two animals, and the control (*Fig. 1*F) and 2 hr LTP (*Fig. 1*G) hemispheres of the other two animals. Three-dimensional reconstructions were made for all of the dendritic spines and synapses occurring along three dendritic segments from each of the control and LTP hemispheres for a total of 24 dendrites and 862 dendritic spines. Axons that were presynaptic to at least 1 of 15 dendritic spines located along the middle of the dendritic segment were traced to determine whether they made more than one synapse along the same dendrite, and thus formed SDSA pairs. All 3D reconstructions and measurements were obtained blind as to condition or animal. *Supplementary Videos 1-4 for 3D illustration of Figs. 1D-G* are provided.

120
121

122
123
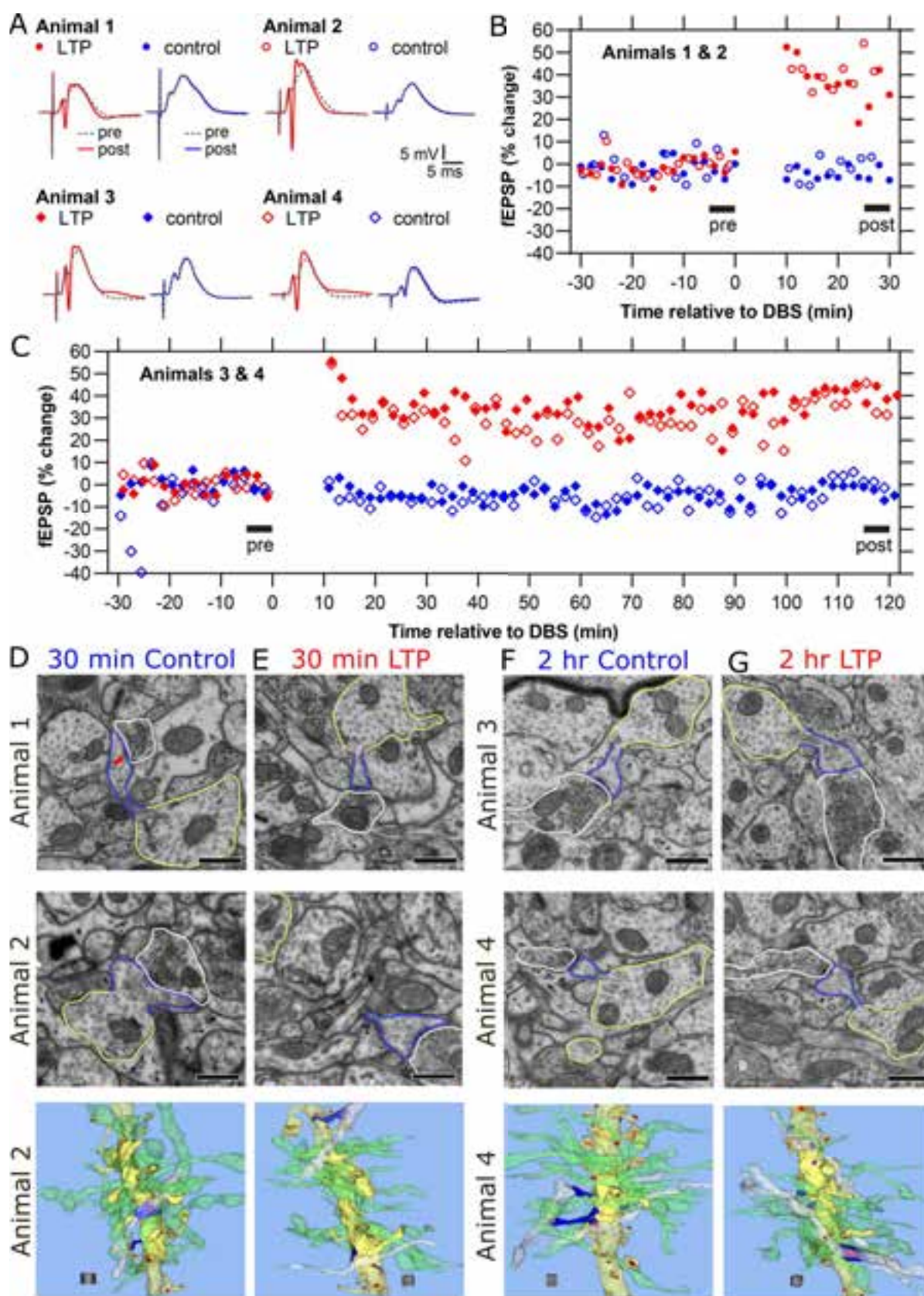
124 Fig. 1: LTP and control responses monitored for 30 min and 2 hours prior to preparation for 3DEM, and representative

125 dendrites from the control and LTP hemispheres in MML.

126 (A) Plots in panel A show representative waveforms from baseline responses (dotted, pre) superimposed on responses
127 following delta-burst stimulation (solid, post) in the LTP (red) or control (blue) hemispheres. (Unique symbols are indicated
128 for each animal and plotted in B and C). (B) Change in fEPSP slopes relative to baseline stimulation in the LTP (red) or
129 control (blue) hemispheres monitored for 30 minutes prior to fixation. The average change relative to baseline stimulation
130 in fEPSP response was 34% and 48% at 30 minutes post-LTP induction and 0% for controls. (C) Change in fEPSP slopes
131 relative to baseline stimulation in the LTP (red) or control (blue) hemispheres monitored for 2 hours prior to fixation. The
132 average change in fEPSP slopes relative to baseline stimulation was 41% and 34% for the LTP (red) and 0% for control
133 (blue) hemispheres. (D-G) Example electron micrographs and 3D reconstructions in the control and LTP hemispheres as
134 indicated for each of the 4 animals. (Scale bars = 0.5 μm.) Bottom row illustrates representative dendrites from control and
135 LTP conditions in Animals 2 and 4 with segment lengths across the row of 9.25, 10.62, 9.44, and 11.33 μm, respectively.
136 Axons synapsing on 15 spines along the middle of the dendrite were analyzed for presynaptic connectivity (solid yellow).
137 Most of the axons (green) made synapses with just one dendritic spine, and some axons (white) made synapses with two
138 dendritic spines (blue). Thus, the white axons illustrate the SDSA pairs. The dendritic shaft and spines occurring along the
139 rest of the reconstructed dendrite are illustrated in translucent yellow. All excitatory synapses are illustrated in red, and the
140 inhibitory synapses in purple. Scale cube = 1 μm^3. ***Supplementary Videos 1-4*** *for 3D illustration of* ***Figs.*** *1D-G* are provided.
141

------

143 **Maintenance of Synaptic Plasticity**
144

145 We analyzed the 4 Dentate Gyrus MML datasets to see how LTP at 30 min and 2 hr post-induction affected spine head
146 volumes. Fig. 2 compares the spine head volume histograms before and after the induction of LTP. Control histograms from
147 the unstimulated hemisphere (***Fig. 2***A, 2B) are presented above their corresponding LTP histograms (***Fig. 2***C, 2D). The
148 differences between the LTP and the control histograms revealed increases in the numbers of both large and small synapses
149 at both time points (***Fig. 2***E). These findings suggest potentiation of stimulated synapses and concurrent depression of
150 presumptive non-stimulated synapses. However, by 2 hours the peaks and troughs shifted such that the increase in smaller
151 spines was transient, and the increase in larger spines was consolidated (***Fig. 2***F). We repeated this analysis for each rat
152 (***Supplementary Fig. 1***). The peaks and troughs of differences between the LTP and the control histograms at both time
153 points were similar to the group averages shown in Fig. 2E-F, confirming the robustness of these findings.
154
155
156
157

5

158
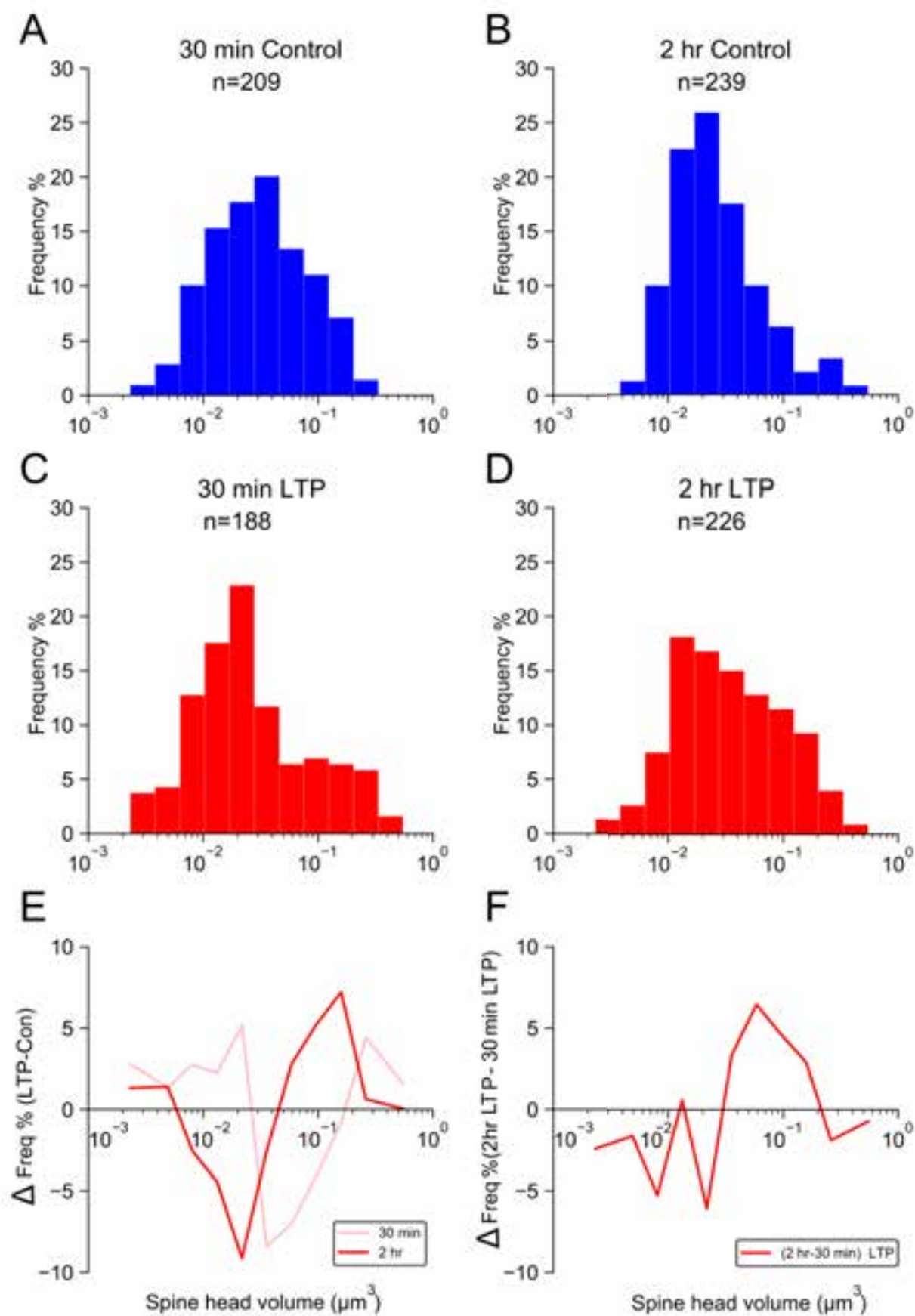
159
160

161 Fig. 2: Change relative to control hemispheres in the distribution of spine head volumes at 30 min and 2 hr after the induction
162 of LTP. (A-D) Frequency distributions of spine head volumes (on log scale) from control and LTP hemispheres as indicated.
163 (E) Difference between the frequency of spine head volumes in control and LTP conditions (i.e., LTP - control) at 30 min
164 (pink curve) and 2 hr (red curve). (F) Difference between the frequency of spine head volumes in 30 min LTP (C) and 2 hr
165 LTP (D) conditions.

166
167
168 **Precision Analysis**
169

170 Precision is defined as the degree of reproducibility of a measurement and is often mistaken for accuracy, which is defined
171 as the deviation of the average measurement from a reference value (*Supplementary Fig. 2*). The CV shown in equation
172 eq 1 is a statistic that measures the variations within a sample, defined by the standard deviation (σ) equation (2), normalized
173 by the mean of the sample (μ), making it a useful metric for measuring precision. Here we used $N = 2$ in equation (2)
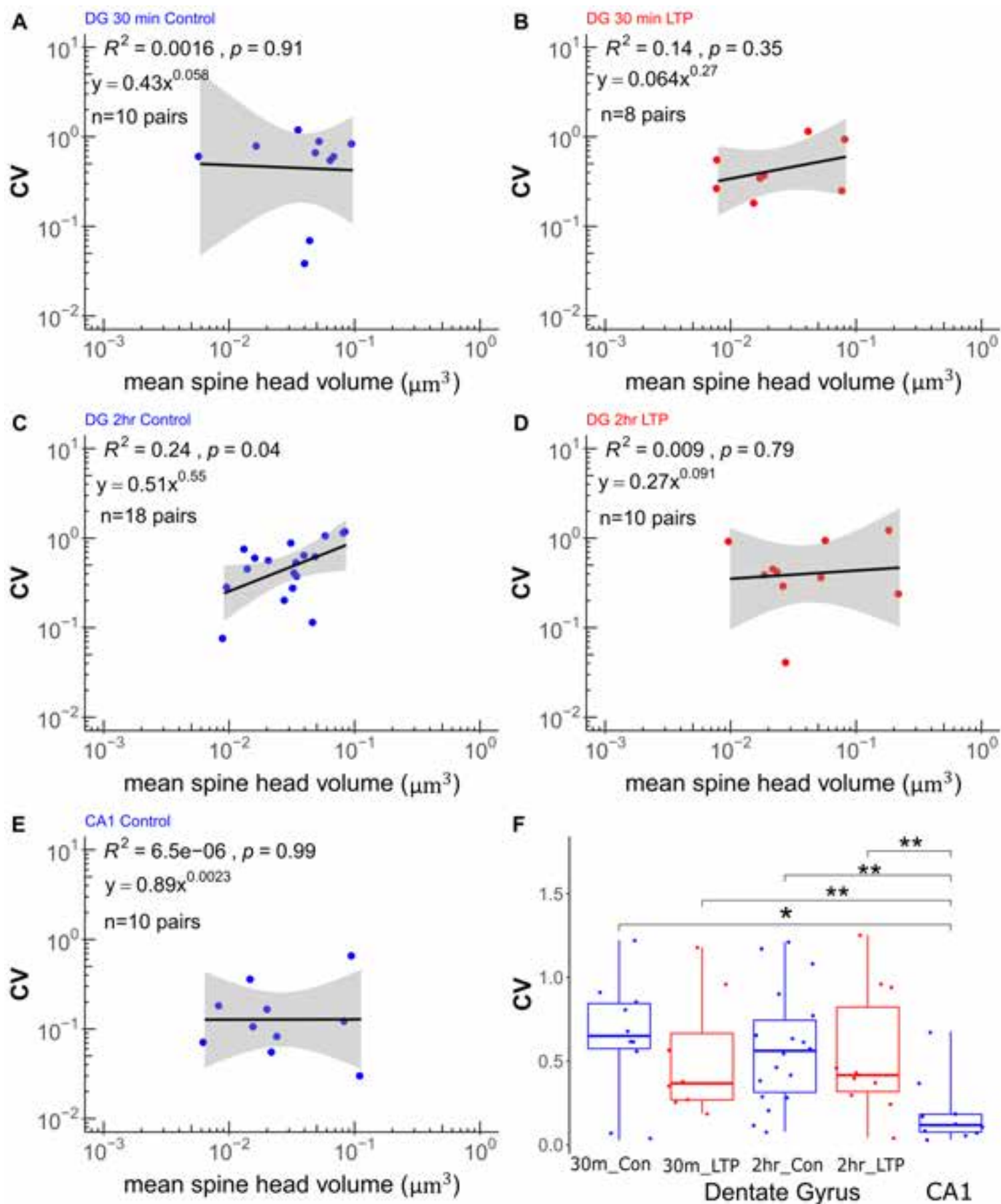174 because we analyzed SDSA pairs.

$$CV = \frac{\sigma}{\mu} \tag{1}$$

$$\sigma = \sqrt{\frac{1}{N-1} \sum_{i=1}^{N} (x_i - \mu)^2} \tag{2}$$

175
176

177 Precision is a key factor for discovering the number of distinguishable states for spine head volumes. First, we determined
178 that the measurement error between investigators of the same spine head volumes was smaller than the variability between
179 the measured spine head volumes of the SDSA spine pairs. Then we could measure the precision of spine head volumes
180 within the SDSA pairs to estimate the precision of synaptic plasticity. We calculated the CV of all SDSA pairs in each of the
181 5 datasets (*Fig. 3*). None of the correlations between the CV values and mean spine head volumes for the SDSA pairs
182 within each condition were significant (except for the noted weak correlation, *Fig. 3*C). These outcomes suggest that the
183 synaptic plasticity based on co-activation history among small spines is as precise as it is for large spines for both control
184 and LTP conditions.

185 In addition, the difference between the CV of SDSA pairs in CA1 was much less (*Fig. 3*E) than in the combined Dentate
186 Gyrus datasets, which did not differ from one another (*Fig. 3*F). Thus, the CV of the SDSA pairs did not differ significantly
187 across the Dentate Gyrus MML conditions but did differ significantly between the two hippocampal regions. The median CV
188 value establishes the precision level of the sets of SDSA pairs in each of the 5 datasets and is used below for cluster analysis
189 and calculation of the number of distinguishable synaptic strength levels. The rationale behind using median CV as a
190 constant threshold for clustering spine head volumes across the range of spine head volumes is our observation that small
191 spines are as precise as large spines for both control and LTP conditions.

A DG 30 min Control

$R^2 = 0.0016$, $p = 0.91$
$y = 0.43x^{0.058}$
n=10 pairs

CV

mean spine head volume (μm^3)

B DG 30 min LTP

$R^2 = 0.14$, $p = 0.35$
$y = 0.064x^{0.27}$
n=8 pairs

CV

mean spine head volume (μm^3)

C DG 2hr Control

$R^2 = 0.24$, $p = 0.04$
$y = 0.51x^{0.55}$
n=18 pairs

CV

mean spine head volume (μm^3)

D DG 2hr LTP

$R^2 = 0.009$, $p = 0.79$
$y = 0.27x^{0.091}$
n=10 pairs

CV

mean spine head volume (μm^3)

E CA1 Control

$R^2 = 6.5e-06$, $p = 0.99$
$y = 0.89x^{0.0023}$
n=10 pairs

CV

mean spine head volume (μm^3)

F

CV

** **
** **
**
*

30m_Con   30m_LTP   2hr_Con   2hr_LTP

Dentate Gyrus   CA1

192
193

8

194 Fig. 3: Analysis of synaptic precision based on CV of SDSA pairs across brain regions and plasticity.

195 (A-E) Same-dendrite same-axon (SDSA) pairs were analyzed from each dataset. The regression line, p value and R^2 for
196 the CV of n SDSA pairs are shown for each indicated condition and hippocampal region. The gray region is the 95%
197 confidence interval for each regression line. The Y axis is the CV for each SDSA pair depicted by blue and red dots in
198 control and LTP conditions, respectively. The X axis shows the mean value of the spine head volumes, on a log scale, for
199 each SDSA pair. (F) Summary values for the Dentate Gyrus and CA1 datasets combined (overall Kruskal-Wallis p-
200 value=0.00085) shows there is a statistically significant difference between the CV of the CA1 SDSA pairs and those in
201 Dentate Gyrus. The one factor KW test (on the first four columns) showed no significant difference between the four Dentate
202 Gyrus conditions (p=0.75). The post-hoc one factor KW tests are done on each combination of CA1 and Dentate Gyrus
203 datasets where asterisks represent significance of the p (*<0.05; **<0.01). Thus, the precision level was significantly higher
204 in area CA1 than Dentate Gyrus, but not significantly different across the Dentate Gyrus conditions.

205

206 **Comparison to Prior Method**

207

208 To introduce and compare the performance of our new method, we reanalyzed the CA1 dataset that was previously
209 analyzed with signal detection theory (***Bartol et al., 2015***). A total of 288 spine head volumes were fully contained within a
210 $6 \times 6 \times 5 \ \mu m^3$ CA1 neuropil volume (***Fig. 4***A). Signal detection theory revealed 26 distinguishable Gaussian distributions
211 with equal CV of 0.12 ± 0.046 (inset, ***Fig. 4***B), and assuming an overlap of 31% (***Fig. 4***B). This amount of overlap is
212 equivalent to assuming a signal-to-noise ratio = 1 and a 69% discrimination threshold common in psychophysics (***Schultz,***
213 ***2007***). Our new clustering method based upon the median CV of the SDSA pairs without any assumptions regarding the
214 signal-to-noise ratio (Algorithms 1 and 2, methods) placed the CA1 spine head volumes into 24 distinguishable categories
215 (***Fig. 4***C). The upper left inset contains 3D reconstructions of the smallest and largest spine head volumes. The largest
216 spine in each cluster is illustrated beneath each bin. The highest frequency occurs in cluster #10, which contains 36 spine
217 head volumes (***Fig. 4***C). Interestingly, there appears to be a second peak at around cluster 21.

218
219
220
221
222
223
224
225
226
227
228
229
230
231
232
233

9

A

0.125 μm³

B
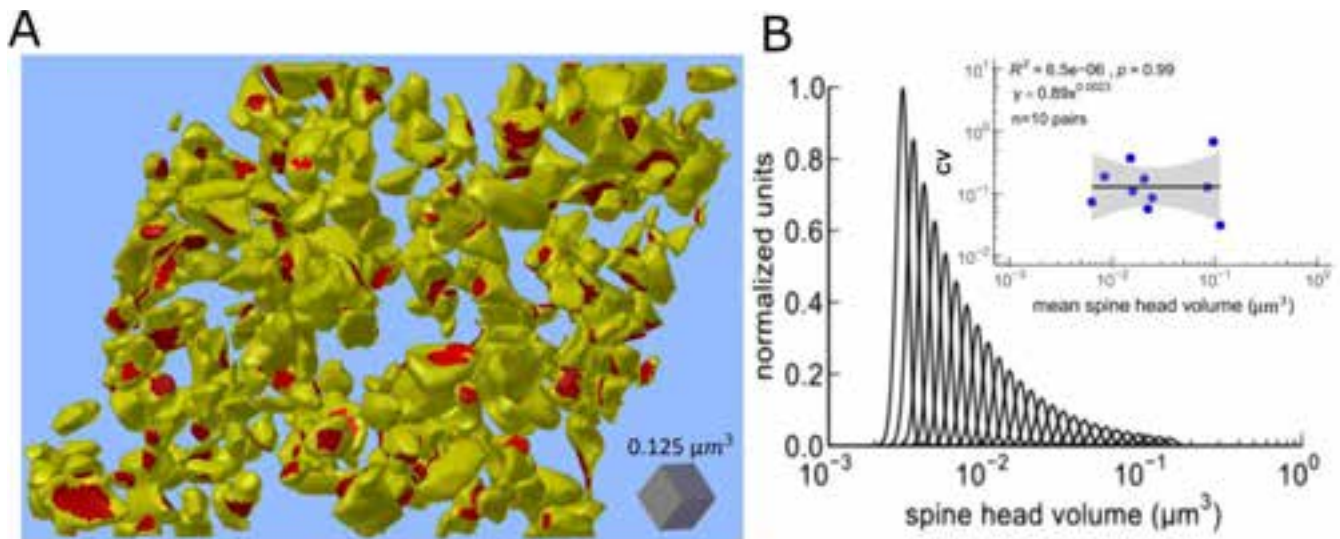
C Histogram of Spine Head Volume Categories (CA1)

234
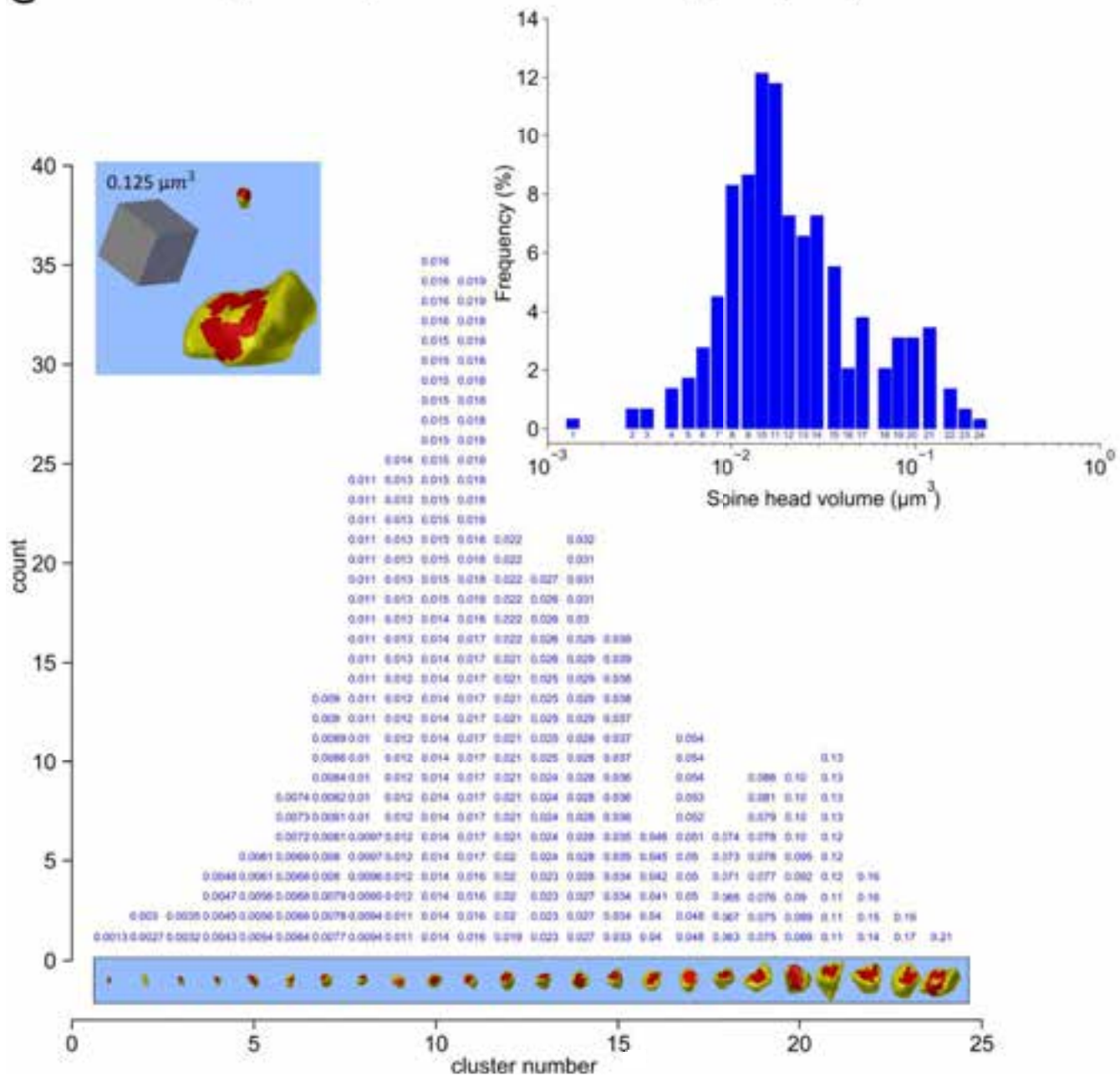
235   Fig. 4: Clustering the spine head volumes from the area CA1 dataset comparing two methods.

236   (A) The 288 spine heads fully captured in the reconstructed volume, displaying the PSD (red) and spine head membrane
237   (yellow). (B) **Bartol et al., 2015** using assumptions from signal detection theory showed that 26 distinguishable Gaussian
238   distributions with equal CV (see inset) and overlap of 31% can span the range of spine head volumes of SDSA pairs
239   equivalent to signal to noise ratio of 1 and 69% discrimination threshold common in psychophysics. (C) Our new clustering
240   algorithm (see Algorithm 2, methods) obtains 24 distinguishable categories of all 288 spine heads in the dataset based on
241   the median CV value. The histogram of spine head volumes in log scale is depicted in the panel C inset. The Y axis shows
242   the number of spine head volumes within each category. The actual spine head volumes of the individual spine heads of a
243   given category are stacked vertically in sorted order for that category. The 3D object shown below each category (vertical
244   column) is the actual 3D reconstructed spine head of the largest head volume in the category. The X axis shows the
245   distinguishable category numbers. All spine head volumes are rounded to two significant digits.

246
247
248   **Number of Distinguishable States in the Dentate Gyrus MML During Plasticity**
249
250   It is important to note that under the previous method, as N is increased the scale range factor (SRF, defined as the ratio
251   of largest spine head volume to the smallest spine head volume) will always increase as the extremes of the distribution
252   are sampled. This outcome will increase the number of Gaussians that span the range but will tend to overestimate the true
253   value of N_C when the population is not continuous. However, under the new method, as N is increased there will be
254   convergence toward the true value of N_C because the true shape of discontinuous distributions are sampled. With the new
255   method we have access to the true frequency of spine head volumes in the clusters, which allows further calculation of the
256   entropy of the distinguishable synaptic strength states, the potential number of modes in the distribution, and the gaps in
257   the range of spine head volumes (bins with no spine head volumes in them).

258   To explore changes in SISC during synaptic plasticity, we applied the new clustering methods to the four Dentate Gyrus
259   MML datasets (**Fig. 5**). The clusters are displayed as histogram bins where each bin is one CV wide. Thus, the CV of spine
260   head volumes within each bin is less than or equal to the median CV found from the SDSA pairs analysis of the specific
261   dataset (see **Fig. 3**, above). The 30 min control and 2 hr control rats had 5 and 6 distinguishable clusters, respectively.
262   Thus, the value of N_C for the control cases were similar despite originating from multiple rats. This closeness between
263   control results validates the repeatability of both the experimental and the computational procedures. At 30 min and 2 hr
264   post-induction of LTP, SISC revealed a higher value of N_C due to both the expansion of the SRF and to the decrease in the
265   CV values (**Table 1**).

266
267
268
269
270
271
272
273
274
275
276
277
278
279

11

280   Table 1: The number of distinguishable states, or categories, (N_C) of spine head volumes.

Dataset Type	# SDSA pairs	Median CV	# Spine head volumes	Median spine head volumes (μm^3)	SRF	N_C
Dentate Gyrus 30 min Control	10	0.65 ± 0.12	209	0.031 ± 0.0037	73	5
Dentate Gyrus 30 min LTP	8	0.37 ± 0.16	188	0.022 ± 0.0014	236	10
Dentate Gyrus 2 hr Control	18	0.56 ± 0.09	239	0.023 ± 0.0013	110	6
Dentate Gyrus 2 hr LTP	10	0.42 ± 0.15	226	0.031 ± 0.0036	141	8
CA1	10	0.12 ± 0.046	288	0.018 ± 0.00091	163	24

281
282   Table 1: For column 3 and 5 the term (± SEM), SEM stands for standard error of median calculated using algorithm 1.

12

283
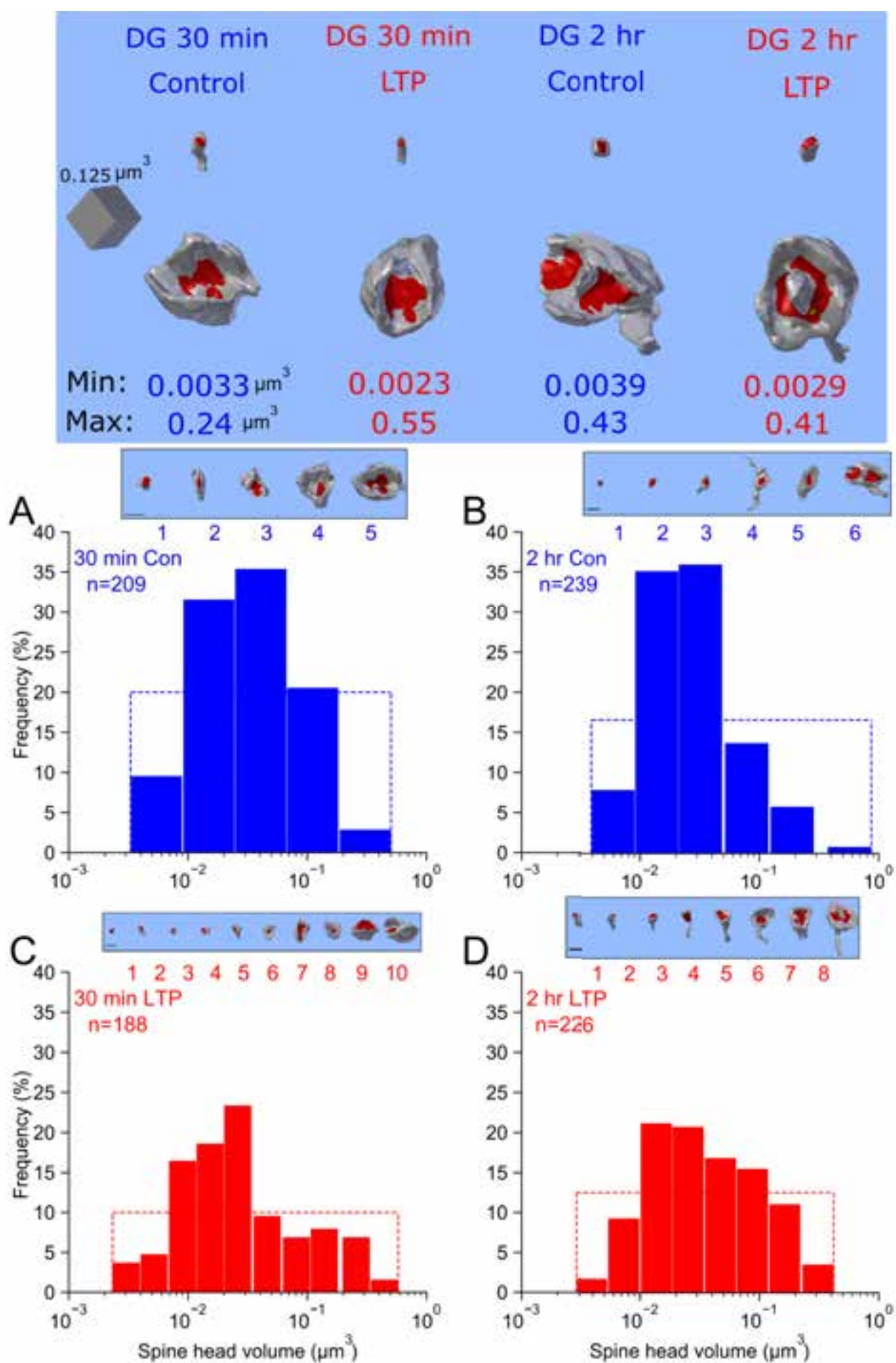
284   Fig. 5: Clustering of spine head volumes in Dentate Gyrus datasets before and after LTP.

285   Clustering algorithm 2 was used, as in Fig. 1C, to show that following LTP there was an increase in N_C. Here categories are
286   illustrated as histogram bins with bin-width equal to the CV shown in Fig. 3. The categories and actual spine head volume
287   values are shown in **Supplementary Fig. 4-7**. Blue and red colors indicate Control and LTP conditions, respectively. For
288   each panel the Y axis shows the counts of spine head volume in the respective bin divided by total number of spine head
289   volumes in the given dataset. The X axis shows the spine head volumes in μm^3 on log scale. (A) Dentate Gyrus 30 min
290   Control, (B) Dentate Gyrus 2 hr LTP, (C) Dentate Gyrus 30 min LTP, (D) Dentate Gyrus 2 hr LTP. The rectangular inset on
291   the top of each histogram shows the largest spine head and category number of each category and aligns with the X axis
292   of the category histogram.
293   For comparison of each histogram to the shape of a uniform distribution, the dashed line indicates the theoretical uniform
294   distribution (and maximum entropy and Shannon information) for the given dataset.

295

296   Shannon Information Storage Capacity of Synapses
297

298   The concept of entropy, H, comes from the field of thermodynamics and measures the amount of uncertainty or disorder,
299   or the number of possible states of a system. Shannon entropy is defined as the average of Shannon information. Shannon
300   entropy measures the amount of information in the set of distinguishable states, each of which has a probability of
301   occurrence. With more information, it is possible to distinguish more states. The Shannon entropy of a discrete random
302   variable is defined as follows:

303

$$H(X) = \mathbb{E}\left[\log_2 \frac{1}{P_X(X)}\right] = \sum_{x \in X} P_X(x) \log_2 \frac{1}{P_X(x)} \tag{3}$$

304

305   Shannon entropy (bits of information) for the 5 datasets are listed in column two of (**Table 2**). These data demonstrate
306   that the synapses are not on/off switches and that the induction of LTP increases the information storage capacity of
307   synapses. (For further detail please see the *Information and Entropy in Synaptic Plasticity* section in Methods)

14

KL Divergence Analysis

Measurement of the distance between an observed distribution, for example spine head volume clusters, and a theoretical uniform distribution with the same number of states is known as the Kullback-Liebler (KL) divergence. A uniform distribution is the maximum entropy discrete probability distribution when there is no constraint on the distribution except having the sum of the probabilities equal 1. Formally, the KL divergence between the distribution of spine head volume clusters (P) and the uniform distribution of states (Q) is the difference in entropy: $[H(P, Q) - H(P)]$. When the distribution of synaptic states is close to uniform, the KL divergence will be low and the Shannon entropy will be maximized. The spine head volume distribution in CA1 is compared with the uniform distribution with 24 states in **Supplementary Fig. 3** and quantified in Table 2.

The maximum entropy and KL divergence were all quite low for all four datasets from the Dentate Gyrus and were around 50% lower than for CA1 (Table 2, column 4; **Supplementary Fig. 3**). The KL divergence for the 30 minute LTP was not different from the control, but the KL divergence for the 2 hour LTP was less than half of its matched control condition (Table 2, column 4). This means that the changes in the distribution of spine head volumes that occurred between 30 minutes and 2 hours shifted toward a more nearly uniform distribution having maximum information due to optimal use of the distinguishable states. The ratio of the KL divergence values over the maximum KL divergence value that could hypothetically occur is a measure of coding efficiency (Table 2, column 5). The lower the ratio, the more efficient the information coding is in the population of synapses. There was a 31% increase in efficiency 30 minutes following LTP and an additional 17% increase after 2 hours. These findings imply that LTP moves distributions of spine head volumes toward maximum information coding and maximum efficiency due to optimal use of the distinguishable states.

Table 2: Calculating the entropy of synaptic weights based on the calculated frequency of distinguishable synaptic states.

Dataset	Shannon Entropy (P)	Maximum Entropy (Q)	KL(P‖Q)	KL / KL$_{MAX}$
Dentate Gyrus 30 min Control	2.0 ± 0.32	2.32 ± 0.34	0.33 ± 0.1	0.14 ± 0.045
Dentate Gyrus 30 min LTP	3.0 ± 0.42	3.32 ± 0.42	0.32 ± 0.089	0.096 ± 0.035
Dentate Gyrus 2 hr Control	2.05 ± 0.27	2.59 ± 0.29	0.53 ± 0.10	0.21 ± 0.040
Dentate Gyrus 2 hr LTP	2.74 ± 0.41	3.0 ± 0.41	0.26 ± 0.086	0.086 ± 0.038
CA1	4.1 ± 0.39	4.6 ± 0.37	0.49 ± 0.068	0.11 ± 0.021

Table 2: For column 2-5 the term (± SE), SE stands for standard error calculated with bootstrapping using algorithm 1 and 2, concurrently.

Discussion

This paper introduces a new analytical approach for determining SISC that has several advantages over our prior approach (**Bartol et al., 2015**). The new method was used on data from area CA1 to compare it with the prior approach. It was then applied to track SISC changes in the Dentate Gyrus at 30 minutes and 2 hours following the induction of LTP. The analyses revealed that synaptic precision, based on covariance of spine head volume in SDSA pairs, was not altered. This finding suggests that as one spine of the pair enlarged (or shrank) following LTP, the other spine head changed in tandem. The number of distinguishable synaptic strengths was increased by LTP by altering the range and frequency of spine head volumes. At 30 minutes, spine head size shifted from the middle of the range both towards smaller and larger sizes. These

15

344 shifts increased the number of bits from 2.0 in the control conditions for both time points to 3.0 bits after 30 min and 2.7 bits
345 at 2 hr following induction of LTP. These outcomes were a consequence of increases in both larger and smaller spine head
346 volumes, which broadened the size distributions, bringing them closer to the optimal uniform Shannon distribution. This
347 broadening in size range was observed in both the 30 min and the 2 hr difference distributions. As a consequence, the
348 information storage capacity was increased by around 50% following LTP, an increase that was preserved between 30 min
349 and 2 hr. However, there was evidence for further reorganization of spine head volumes after 30 min since the KL
350 divergence between the distribution of spine head volumes and the optimal uniform distribution at 2 hr was half that of the
351 control, thereby using the range of spine head volume sizes more efficiently.

352

Advantages of the new SISC analysis

354 There are several advantages to the new SISC method for assessing the storage capacity of synapses. Signal detection
355 theory assumed that the width of the Gaussian curves, based on the CV of the SDSA pairs, were distributed equally along
356 the full range of sampled spine head volumes, without accounting for gaps in the distribution. Thus, the signal detection
357 theoretical approach tended to overestimate the true number of distinct synaptic states because the distribution of the
358 population was assumed to be continuous. In the new SISC analysis, the number of distinct synaptic states defined by the
359 individual clusters converges toward the true number of states as the number of spine head volumes increases, and the
360 true shape of a possibly discontinuous distribution is sampled. A second advantage is that the full population of spine head
361 volumes, not just the SDSA pairs, are included in the analysis, greatly improving the statistical power of the estimate. A
362 third advantage is that there are no free parameters in the estimate, unlike signal detection theory where the degree of
363 overlap of the Gaussians is a free parameter. Finally, information theory allows access to the frequency of the clusters,
364 making it possible to compute the entropy of the distinguishable synaptic strengths, the number of modes in the distribution,
365 and any gaps in the range of functionally distinguishable synaptic strengths.

366

Information Theory of Synapses

368 The actual distribution of synaptic states found by our novel clustering algorithm could also be compared with a uniform
369 distribution — the distribution having maximum entropy as an upper bound — to explore the efficiency of coding after LTP.
370 The postsynaptic dendrite or soma is the receiver, which has to distinguish the strengths of messages coming from discrete
371 synaptic inputs. The distinguishability of the messages depends on the precision with which synaptic plasticity sets the
372 strength of individual synapses. Information theory allowed us to quantify the precision and information content of the
373 message. Following LTP, the weight distributions were closer to uniform and hence closer to the upper bound for the
374 calculated value of N_C. We have shown that the amount of information represented by synaptic weights in neural circuits can
375 be quantified by the distinguishability of synaptic weights. Here "distinguishability" fundamentally depends on the precision
376 of the synaptic weights. When the precision of synaptic weights is low, the amount of information that can be stored in the
377 ensemble of the neurons will also be low. Complete absence of precision implies a random process for setting synaptic
378 weight and no information stored at synapses. Because spine head volume is highly correlated with synapse size (***Bartol et***
379 ***al., 2015***), the precision of spine head volumes can be used to measure the distinguishability of the synaptic weights. High
380 precision yields a greater number of distinguishable spine head volume clusters and hence higher information storage
381 capacity. The number of distinguishable weights is not static but varies with the history of synaptic plasticity and is different
382 in different parts of the brain. Thus, the amount of information that a population of synapses can store is not fixed but can be
383 expanded toward the Shannon limit.

Comparison to Synapses in the Cerebral Cortex

SDSA pairs are a type of "joint synapse," but note that joint synapses have a broader definition — namely, *multiple synapses* sharing the same pre- and postsynaptic *neurons*, not just the same axon and the same dendrite. Joint synapses with up to 7 shared synapses across the entire neuron have been found in other 3DEM studies (***Dorkenwald et al., 2019***), (***Motta et al., 2019***). The surface area of the axon-spine interface (ASI), not spine head volume, was measured in layer 4 of somatosensory cortex in ***Motta et al.*** (2019). Motta et al. noted that saturating LTP or LTD could explain the lower CV (higher level of precision) observed among spines with the largest or smallest ASI. However, they also observed higher CV among spines with intermediate sized ASI, which is inconsistent with our findings in ***Fig. 3***. Perhaps this difference can be attributed to their measurement of ASI, which may depend on aspects of synaptic function other than synaptic weight.

In another study of pyramidal neurons in cortical layer 2/3 (***Dorkenwald et al., 2019***), spine head volumes were similar among pairs that shared the same axon but were on different dendrites from the same cell. The distribution of spine head volumes in their sample had two broad peaks, suggesting that the populations of small and large synapses were distinct. Similarly, despite the small numbers there may be two distinct peaks in our distribution of spine head volumes in area CA1. The frequency of small spines is much higher than larger spines, consistent with the observations that small spines are generally more transient than the larger, typically more stable spines (***Holtmaat et al., 2009***). Indeed, in adult hippocampal area CA1, small spine outgrowth is stalled while synapses on the largest stable spines further enlarge following LTP (***Bell et al., 2014***).

Conclusion

This paper explored the precision of synaptic plasticity and our analyses revealed new principles for information coding. Information coding in neural circuits has multiple substrates over a wide range of spatial and temporal scales. How information is coded, and its potential efficiency depends on how the information is stored. Here we measured efficiency by analyzing the number of distinguishable categories for synaptic weights and their distributions. Based on the calculation of Kullback–Leibler divergence between the distributions of synaptic weights and that of uniform weights (which is an upper bound for the maximum entropy), we found that coding by synaptic sizes is highly efficient, meaning that the synapses and their acquired synaptic weights are efficiently spread across the distinguishable bins. Moreover, at 2 hr post-induction of LTP (after the new weights have stabilized), the KL divergence between the synaptic distributions and the corresponding uniform distribution is reduced by 50% in comparison to 30 min post-induction of LTP. This suggests that after synaptic plasticity has been initiated, the distribution of synaptic weights further evolves toward a more uniform distribution to maximize the entropy of the distribution and hence maximize the information content. Our analysis has revealed a new way that the late phase of LTP may be involved in shifting the distribution of spine head volumes to achieve more efficient use of coding space in the available synaptic population.

17

Methods

The list of manuscript abbreviations:

Term	Abbreviation
Synaptic Information Storage Capacity	SISC
Long-term Potentiation	LTP
Postsynaptic Density	PSD
Same Dendrite Same Axon	SDSA
Coefficient of Variation	CV
Kullback-Leibler divergence	KL divergence
field Excitatory Postsynaptic Potential	fEPSP

The methods used to prepare the CA1 3DEM dataset are described in *Bartol et al., 2015*. Here we present the details of experimental protocols used to prepare 3DEM datasets for 30 min and 2 hours post induction of LTP in Dentate Gyrus of 4 rats. Explanations are adapted from *Bromer et al., 2018* describing the 30 min control and LTP datasets, and presented here for the first time are the protocols for 2 hours post induction of LTP.

Surgery and Electrophysiology (Dentate Gyrus)

The 30 min dataset was collected from two adult male Long-Evans rats aged 121 and 179 d at the time of LTP induction and perfusion. The 2 hour dataset was collected from two adult male Long-Evans rats aged 150 and 170 d at the time of LTP induction and perfusion. It is worth noting that the histograms in *Fig. 2*A,D and *Fig. 2*B,E are made for the combined datasets from the two 30 min datasets for control and LTP conditions, and the two 2 hour datasets for control and LTP conditions, respectively.

The animals were surgically implanted as previously described in *Bowden et al., 2012* with wire stimulating electrodes separately into the medial and lateral perforant pathways running in the angular bundle in the LTP hemisphere, and in the medial perforant pathway only in the control hemisphere (only medial path data are described in this paper). Wire field excitatory postsynaptic potential (fEPSP) recording electrodes were implanted bilaterally in the dentate hilus. Two weeks after surgery, baseline recording sessions (30 min and 2 hours) commenced, with animals being in a quiet alert state during the animals' dark cycle. Test pulse stimuli were administered to each pathway as constant-current biphasic square-wave pulses (150 μs half-wave duration) at a rate of 1/30 s, and alternating between the three stimulating electrodes. The test pulse stimulation intensity was set to evoke medial path waveforms with fEPSP slopes > 3.5 mV/ms in association with population spike amplitudes between 2 and 4 mV, at a stimulation current ≤ 500 μA. On the day of LTP induction, after stable baseline recordings were achieved, animals received 30 min of test pulses followed by delta-burst stimulation delivered to the ipsilateral medial perforant path, while the contralateral hippocampus served as a control. The LTP-inducing delta-burst stimulation protocol consisted of five trains of 10 pulses (250 μs half-wave duration) delivered at 400 Hz at a 1 Hz interburst frequency, repeated 10 times at 1 min intervals (*Bowden et al., 2012*). Test pulse stimulation then resumed until the brains were obtained at 30 min and 2 hours after the onset of delta-burst stimulation. The initial slope of the medial

18

452 path fEPSP was measured for each waveform and expressed as a percentage of the average response during the last 15
453 min of recording before delta-burst stimulation.

454
455 **Perfusion and Fixation (Dentate Gyrus)**
456
457 At 30 min after the commencement of delta-burst stimulation, animals were perfusion-fixed under halothane anesthesia and
458 tracheal supply of oxygen (***Kuwajima et al., 2013***). The perfusion involved brief (~20 s) wash with oxygenated Krebs-Ringer
459 Carbicarb buffer [concentration (in mM): 2.0 $CaCl_2$, 11.0 D-glucose, 4.7 KCl, 4.0 $MgSO_4$, 118 NaCl, 12.5 Na_2CO_3, 12.5
460 $NaHCO_3$; pH 7.4; osmolality, 300–330 mmol/kg], followed by fixative containing 2.0% formaldehyde, 2.5% glutaraldehyde
461 (both aldehydes from Ladd Research), 2 mM $CaCl_2$, and 4 mM $MgSO_4$ in 0.1 M cacodylate buffer (pH 7.4) for ~1 hr (~1,900
462 mL of fixative was used per animal). The brains were removed from the skull at about 1 hr after end of perfusion, wrapped
463 in several layers of cotton gauze, and shipped on ice in the same fixative from the Abraham Laboratory in Dunedin, New
464 Zealand, to the laboratory of K.M.H. in Austin, Texas by overnight delivery (TNT Holdings B.V.).

465
466 **Tissue Processing and Serial Sectioning (Dentate Gyrus)**
467
468 The fixed tissue was then cut into parasagittal slices (70 μm thickness) with a vibrating blade microtome (Leica
469 Microsystems) and processed for electron microscopy as described previously (***Kuwajima et al., 2013***), (***Harris et al.,***
470 ***2006***). Briefly, the tissue was treated with reduced osmium (1% osmium tetroxide and 1.5% potassium ferrocyanide in 0.1
471 M cacodylate buffer) followed by microwave-assisted incubation in 1% osmium tetroxide under vacuum. Then the tissue
472 underwent microwave-assisted dehydration and en bloc staining with 1% uranyl acetate in ascending concentrations of
473 ethanol. The tissue was embedded into LX-112 epoxy resin (Ladd Research) at 60° C for 48 hr before being cut into series
474 of ultrathin sections at the nominal thickness of 45 nm with a 35° diamond knife (DiATOME) on an ultramicrotome (Leica
475 Microsystems). The serial ultrathin sections from MML (region of molecular layer ~125 μm from top of granule cell layer in
476 dorsal blade of the hippocampal dentate gyrus) were collected onto Synaptek Be-Cu slot grids (Electron Microscopy
477 Sciences or Ted Pella), coated with Pioloform (Ted Pella), and stained with a saturated aqueous solution of uranyl acetate
478 followed by lead citrate (***Reynolds, 1963***).

19

Imaging and Alignment (Dentate Gyrus)

The serial ultrathin sections were imaged, blind as to condition, with either a JEOL JEM-1230 TEM or a transmission-mode scanning EM (tSEM) (Zeiss SUPRA 40 field-emission SEM with a retractable multimode transmitted electron detector and ATLAS package for large-field image acquisition; (**Kuwajima et al., 2013**)). On the TEM, sections were imaged in two-field mosaics at 5,000× magnification with a Gatan UltraScan 4000 CCD camera (4,080 pixels × 4,080 pixels), controlled by DigitalMicrograph software (Gatan). Mosaics were then stitched with the photomerge function in Adobe Photoshop. The serial TEM images were first manually aligned in Reconstruct (**Fiala JC., 2005**; synapseweb.clm.utexas.edu/software- 0) and later in Fiji with the TrakEM2 plugin (refs. (**Fiala JC., 2005; Cardona A, et al., 2012; Schindelin J, et al., 2012)**; fiji.sc). On the tSEM, each section was imaged with the transmitted electron detector from a single field encompassing 32.768 μm × 32.768 μm (16,384 pixels × 16,384 pixels at 2 nm/pixel resolution). The scan beam was set for a dwell time of 1.25–1.4 ms, with the accelerating voltage of 28 kV in high-current mode. Serial tSEM images were aligned automatically using Fiji with the TrakEM2 plugin. The images were aligned rigidly first, followed by application of affine and then elastic alignment. Images from a series were given a five letter code to mask the identity of experimental conditions in subsequent analyses with Reconstruct. Pixel size was calibrated for each series using the grating replica image that was acquired along with serial sections. The section thickness was estimated using the cylindrical diameters method (**Fiala et al., 2001**).

Unbiased Reconstructions and Identification of SDSA Pairs (Dentate Gyrus)

Three dendrites of similar caliber were traced through serial sections from each of the two control and two LTP hemispheres for a total of six dendrites per condition (with a total of 24 dendrites for the 30 min and 2 hr datasets). Dendrite caliber previously has been shown to scale with dendrite cross-sectional area and microtubule count (**Harris et. al., 2022**). The microtubule count ranged from 30 to 35 and represents the average among all dendrites found in the MML of dentate gyrus. These dendritic segments ranged in length from 8.6 to 10.6 μm for the six control dendrites and 9.3 to 10.6 μm for the six LTP dendrites. Contours were drawn using Reconstruct software on serial images for each spine head. PSDs were identified by their electron density and presence of closely apposed presynaptic vesicles. A total of 209 spines were complete along the control dendrites and 188 spines were complete along the LTP dendrites. These were used for the indicated analyses. The unbiased dendritic segment analysis involved assessing the number of synapses, SDSAs, and axons interacting with each dendritic segment. Beginning in the center of each of the 24 dendrites, the presynaptic axons were traced past the nearest neighboring axonal bouton until they were determined to form synapses with the same dendrite or a different dendrite. Only the middle portion of the dendrite lengths could be used because only spines in the middle of the dendrite had presynaptic axons sufficiently complete within the series to determine their connectivity. In three cases, one axon made synapses with dendritic spines from two different dendrites in our sample, and these three were included for both dendritic segments. Each of the 24 dendrites (12 for 30 min and 12 for the 2 hr datasets) was truncated to contain the central 15-20 spine and shaft synapses with known connectivity. The z-trace tool in Reconstruct was used to obtain the unbiased lengths spanning the origin of the first included spine to the origin of the first excluded spine (**Fiala et al., 2001**). The lengths ranged from 2.8 to 5.9 μm for the six control dendrites and 3.1 to 6.1 μm for the six LTP dendrites. Then the number per micrometer length of dendrite was computed for spines, axons, and SDSAs. PSD areas were measured in Reconstruct according to the orientation in which they were sectioned (**Harris et al., 2015**). Perfectly cross-sectioned synapses had distinct presynaptic and postsynaptic membranes and synaptic cleft, and their areas were calculated by summing the product of PSD length and section thickness for each section spanned. In face synapses were cut parallel to the PSD surface, appeared in one section, and were measured as the enclosed area on that section. Obliquely sectioned PSDs were measured as the sum of the total cross-sectioned areas and total en face areas without overlap on adjacent sections. Then the synapse areas were summed along the truncated, unbiased dendritic length to compute values.

Segmentation and Evaluation of Spines (Dentate Gyrus)

Blender, a free, open-source, user-extensible computer graphics tool, was used in conjunction with 3D models generated in Reconstruct. We enhanced our Python add-on to Blender, Neuropil Tools (***Bartol et al., 2015***), with a new Processor Tool to facilitate the processing of the 3D reconstruction and evaluation of spines. The additions encompassed in Processor Tool were as follows:

i) The software allows for the selection of traced objects from Reconstruct (.ser) files by filter, allowing the user to select only desired contour traces (in this case spine head and PSD contours for three dendrites per series).

ii) At the press of a button, the tool generates 3D representations of selected contours in Blender. This step invokes functions from VolRoverN (***Edwards et al., 2014***) from within Blender to generate mesh objects by the addition of triangle faces between contour traces.

iii) Smoothing and evening of the surface of spine objects is accomplished with GAMer software (fetk.org/codes/gamer/).

iv) In a few cases, the formation of triangles was uneven and required additional manipulation by Blender tools and repeating of step iii before proceeding to step v.

v) Finally, the PSD areas are assigned as metadata (represented by red triangles) for the reconstructed spine heads.

This assignment is performed based on the overlap of PSD and spine head contours (described above) in 3D space. Dendritic spines were segmented as previously described (***Bartol et al., 2015***) using the Neuropil Tools analyzer tool. We chose to measure spine volumes because at present they can be more accurately measured than other correlated metrics — synaptic area and vesicle number (***Bartol et al., 2015***). The edges of the synaptic contact areas are less precisely determined in oblique sections, and vesicles can be buried within the depth of a section or span two sections and hence are less reliably scored. The selection of spine head from spine neck and from spine neck to dendritic shaft were made using the same standardized criterion as before (visually identified as halfway along the concave arc as the head narrows to form the neck). Spines were excluded if they were clipped by the edge of the image dataset. To ensure the accuracy of the measurements, segmentation of the spine head volume was performed four times (twice each by two people) and averaged. A further check was added at this step, whereby spine heads with a $CV \geq 0.02$ for all four measurements were visually evaluated by an expert, and any discrepancy in the segmentation was corrected. Interestingly, the only spines with a CV larger than 0.02 were in the LTP condition. We believe this occurs because the spines undergoing LTP are likely to be in transition at the 30 min time point, and as such the delineation between spine head and spine neck is more difficult to distinguish. In the two control condition series, further evaluation by an expert was performed, and adjustments were made accordingly (Fig. 2 and Fig. S4 in (***Bromer et al., 2018***)).

Data & Code Availability

The data and codes used in the present study will be available in the following github link:
https://github.com/MohammadSamavat

Statistical Analysis

Statistical analysis and plots were generated using Python 3.4 with NumPy, SciPy, and Matplotlib. Fig. 3 is made by R programming packages as follows: ggplot2, scales, xlsx, ggpmisc. RStudio.

In order to show the empirical distribution of spine head volumes for the 4 Dentate Gyrus datasets, we illustrated the 4 Dentate Gyrus spine head volume histograms in Fig. 2. For panel A-D the Y axis shows the frequency of spine head volumes within each of the bins and the X axis shows the bins start and end points. To get the bins' start and end points, the range of the 4 datasets were divided into 11 equal width bins in logarithmic scale (Fig. 2 panel A-D).

For the precision analysis we used the coefficient of variation (equation 1) as a metric to show the precision level by calculating the ratio of standard deviation (equation 2) over the mean of N joint synapses. Here N is 2 but can take higher values as up to 7 have been detected in previous studies. Since this is a sample from the unknown population of joining synapses, we used the corrected standard deviation formula with 1/(N-1) factor.

The coefficient of determination, denoted R^2, was used in Fig. 3 panel A-E to show the proportion of the variation in the dependent variable (CV) that is predictable from the independent variable (spine head volumes).

One factor Kruskal-Wallis (KW) test was in Fig. 3F to check for a significant difference between the 4 Dentate Gyrus SDSA datasets and the CA1 dataset.

Lognormal transform of data was in analyses of skewed distributions (Fig. 2 A-F. Fig. 3, A-E. Fig. 4 B and C. Fig. 5 A-D.)

Bootstrapping was done by combining algorithms 1 and 2 to calculate the standard errors as explained below in the sections *Standard error of Median* and *Clustering Algorithm*.

The standard errors of the entropy, efficiency constant, maximum entropy for uniform distribution, and KL divergence (Table 2 column 2-5) are all calculated similarly using the bootstrapping technique explained in algorithm 1. (Please see (Efron et al., 2021) for further information regarding bootstrapping for the calculation of standard error.)

Standard error of Median

The standard error of median for the precision levels of each of the 5 dataset's SDSA pairs is calculated with Algorithm 1 as follows. The idea is to generate 1000 bootstrap samples of length n, each sampled from the n SDSA pairs with replacement, to estimate the standard error of median for the n SDSA pairs (Table 1, column 3). The standard error of median of spine head volumes follows the same procedure using Algorithm 1.

Algorithm 1 Bootstrap Algorithm for Estimating the Standard Error of Median

Require: $n \geq 1$

Let $X_1, \ldots, X_n$ be some data and $\hat{\theta}_n = t(X_1, \ldots, X_n)$

For $b = 1, \ldots, B$

Simulate $X_1^{*(b)}, \ldots, X_n^{*(b)} \overset{iid}{\sim} F_n$ by sampling with replacement from $\{X_1, \ldots, X_n\}$

Evaluate $\hat{\theta}_n^{*(b)} = t(X_1^{*(b)}, \ldots, X_n^{*(b)})$

$$\hat{\sigma}_{n,B}^2 = \frac{1}{B} \sum_{b=1}^{B} \left(\hat{\theta}_n^{*(b)} - \frac{1}{B} \sum_{b=1}^{B} \hat{\theta}_n^{*(b)} \right)^2$$

Return the bootstrap estimate of standard error of median

$$\hat{\sigma}_{n,B}$$

Clustering Algorithm

To construct the clusters, spine head volumes are sorted from smallest to the largest. The first value (smallest value) is selected and the CV of that value and the remaining head volumes are calculated in a pairwise manner. The head volumes for which the calculated CV is below the threshold (the median value of the SDSA pairs CV) are assigned to the first category and deleted from the pool of N spine head volumes. This procedure is repeated until the CV exceeds the median SDSA pairs CV and a new category is formed. New categories are formed until all the remaining spine head volumes are assigned to a category and the original vector of spine head volumes is empty (see Algorithm 2 for details). It is guaranteed that the coefficient of variation between each random pair within each category is less than the threshold value measured from the reconstructed tissue SDSA pairs. All spine head volumes are rounded to two significant digits for the display.

Algorithm 2 Clustering Algorithm

1: **function** Precision Calculation (Same Dendrite Same Axon pairs ($SDSA$), N pairs (a,b) of spine head volumes)

2:     **for** $a, b \in SDSA[i]$ i in 1:N **do**

3: $cv = \sigma(a,b) / \mu(a,b)$

4: $cv[i] = cv$

5:     **end for**

6:     **return** {Precision_Level=$Median(cv)$}

7: **end function**

8: **function** Clustering spine head volumes (shv vector)

9:     Sort shv s.t. $shv[i] < shv[i+1]$

10:     $L = Length(shv)$

11:     $List\_of\_shcluster = NULL$

12:     **while** $Length(shv) \neq 0$ **do**   ▷ Here we do the clustering with the median value of SDSA pairs calculated with the above function.

13:         a= $shv[1]$

14:         **for** every $b \in shv[k]$ where K in 2:L **do**

15:             Cluster=NULL

16:             **if** $cv(a, b) < Median(CV)$ **then**

17:                 $Cluster \leftarrow b$

18:             **end if**

19:         **end for**

20:         $List\_of\_shcluster[j] \leftarrow Cluster$

21:         $shv = shv[-Cluster]$ (deleting the spine head volumes stored in cluster j from the shv vector)

22:         j=j+1

23:     **end while**

24:     **return** {$List\_of\_shcluster$, N$_C$ = j-1} (List of clusters and number of clusters.)

25: **end function**

23

640

641   For each panel in Fig. 5, the Y axis shows the percentage of spine head volumes counts in the respective bin. The area
642   under each plot is normalized to *1* for a fair comparison. The X axis shows the spine head volumes in μm^3 on the log scale.
643   The width of each bin is exactly the median value of the set of CV values for each condition calculated in Fig. 3 (Example:
644   for bin-1 panel-1 [x1,x2], CV(x1,x2)=0.65, where x1 is the smallest spine head volume in Dentate Gyrus 30 min control
645   dataset and x2 is a larger hypothetical head volume that has a CV of 0.65 with x1). The height of bin 1 is the number of
646   spine head volumes in that range normalized to the total number of spine head volumes in that dataset (Example: for Fig.
647   5A for Dentate Gyrus 30 min control it is 236). (A) Dentate Gyrus 30 min control. (B) Dentate Gyrus 2hr LTP. (C) Dentate
648   Gyrus 30 min LTP. (D) Dentate Gyrus 2hr LTP.

649

650   **Information and Entropy in Synaptic Plasticity**

651   "The fundamental problem of communication is that of reproducing at one point either exactly or approximately a message
652   selected at another point. Frequently the messages have meaning; that is they refer to or are correlated according to some
653   system with certain physical or conceptual entities. These semantic aspects of communication are irrelevant to the
654   engineering problem. The significant aspect is that the actual message is one selected from a set of possible messages.
655   The system must be designed to operate for each possible selection, not just the one which will actually be chosen since
656   this is unknown at the time of design." (Shannon*, 1948*)

657

658   Shannon's information theory is the rigorous basis for a new method to quantify empirically SISC; that is, the number of bits
659   of Shannon entropy stored per synapse. For this new method, only the precision as measured by the coefficient of variation
660   (CV) of SDSA pairs, illustrated in Fig. 3, was borrowed from Bartol et al. (2015). The new method performs non-overlapping
661   cluster analysis (Fig.s 4 and 5) using Algorithm 2, to obtain the number of distinguishable categories of spine head volumes
662   from the CV measured across the reconstructed dendrites.

663

664   The Shannon information per synapse is calculated by using the frequency of spine head volumes in the distinguishable
665   categories where each category is a different message for the calculation of Shannon information. The maximum number
666   of bits is calculated as the $log_2(N_C)$ where N_C is the number of categories which set an upper bound for the SISC.

667

668   When calculating the amount of entropy per synapse, the random variable is the synapse size and the number of
669   distinguishable synaptic states is the realization of a random variable for the occurrence of each state. The probability of the
670   occurrences of each state is calculated by the fraction of the number of spine head volumes in each of the clusters over the
671   total number of spine head volumes in the reconstructed volume.

672

673   The information coding efficiency at synapses is measured by Kullback-Leibler (KL) divergence to quantify the difference
674   between two probability distributions, one from the categories of spine head volumes and the other from a corresponding
675   uniform distribution with the same number of categories.

676

677

678

679

680   **Synaptic Information Storage Capacity**

681

682   Spine morphology has substantial variation across the population and lifetime of synapses. Hebbian plasticity puts forth a
683   causal relationship and transformation of information from the presynaptic site to the postsynaptic site by the adjustment of
684   efficacy of synaptic transmission, or "synaptic weight." The pattern of synaptic weights in the ensemble of neural circuits
685   allows us to define both information and the recipient of the message in the context of synaptic plasticity. The recipient of

686 the message is the neural ensemble or the pattern of synaptic weights that store the message and read the message during
687 the recall process, which is the reactivation of the synaptic weights in the memory trace. The amount of information is
688 quantified by the distinguishability of synaptic weights which comprise the memory trace. Here "distinguishability" implies
689 that the precision of synaptic weights play a significant role.
690
691 The synapse is the unit of information storage in an ensemble of neurons, and if the precision level of synaptic weights is
692 low then the amount of information that can be stored per synapse and in the ensemble of the neurons will also be low.
693 Because the spine head volume is highly correlated with synapse size, the precision of spine head volumes can be used to
694 measure the distinguishability of the synaptic weights. High precision yields a greater number of distinguishable categories
695 (i.e. states or clusters) for spine head volumes and hence higher information storage capacity.

Author contributions

M.S., T.M.B., W.C.A., K.M.H, and T.J.S. designed research; M.S., T.M.B., W.C.A., K.M.H., and T.J.S., analyzed data; M.S., designed and implemented all simulation algorithms and generated results for the manuscript and applied the information theory to the analyses with contributions from T.M.B., W.C.A., K.M.H. and T.J.S.; M.S., T.M.B., J.B.B., D.D.H., D.C.H., P.V.G., M.K., J.M.M., P.H.P., W.C.A., K.M.H, and T.J.S. performed research; J.B.B., M.K., J.M.M., W.C.A., and K.M.H. designed and performed the electrophysiology experiments, tissue processing, and imaging; M.S., C.B., J.B.B., D.D.H., D.C.H., P.V.G., M.K., P.H.P., and K.M.H. performed, curated reconstructions; M.K. and D.D.H. made martials for Fig. 1; M.S. and T.J.S. wrote the paper with contributions from T.M.B., W.C.A., K.M.H. This research is part of multi-institutional collaboration project NeuroNex 1 & 2 led by K.M.H.

References

Bartol TM, Bromer C, Kinney J, Chirillo MA, Bourne JN, Harris KM, Sejnowski TJ. Nanoconnectomic upper bound on the variability of synaptic plasticity. Elife. 2015; 4:e10778.

Bowden JB, Abraham WC, Harris KM. Differential effects of strain, circadian cycle, and stimulation pattern on LTP and concurrent LTD in the dentate gyrus of freely moving rats. Hippocampus. 2012; 22(6):1363–1370.

Bromer C, Bartol TM, Bowden JB, Hubbard DD, Hanka DC, Gonzalez PV, Kuwajima M, Mendenhall JM, Parker PH, Abraham WC, et al. Long-term potentiation expands information content of hippocampal dentate gyrus synapses. Proceedings of the National Academy of Sciences. 2018; 115(10):E2410–E2418.

Buchs PA, Muller D. Induction of long-term potentiation is associated with major ultrastructural changes of activated synapses. Proceedings of the National Academy of Sciences. 1996; 93(15):8040–8045.

Ramón y Cajal S. The Croonian lecture.—La fine structure des centres nerveux. Proceedings of the Royal Society of London. 1894; 55(331-335):444–468.

Dorkenwald S, Turner NL, Macrina T, Lee K, Lu R, Wu J, Bodor AL, Bleckert AA, Brittain D, Kemnitz N, et al. Binary and analog variation of synapses between cortical pyramidal neurons. bioRxiv. 2019; .

Harris KM, Stevens JK. Dendritic spines of CA 1 pyramidal cells in the rat hippocampus: serial electron mi - croscopy with reference to their biophysical characteristics. Journal of Neuroscience. 1989; 9(8):2982–2997.

Kuwajima M, Mendenhall JM, Harris KM (2013) Large-volume reconstruction of brain tissue from high-resolution serial section images acquired by SEM-based scanning transmission electron microscopy. Methods Mol Biol 950:253–273.

Harris KM, et al. (2006) Uniform serial sectioning for transmission electron microscopy. J Neurosci 26:12101–12103.

Reynolds ES (1963) The use of lead citrate at high pH as an electron-opaque stain in electron microscopy. J Cell Biol 17:208–212.

Fiala JC (2005) Reconstruct: A free editor for serial section microscopy. J Microsc 218: 52–61. 48.

Cardona A, et al. (2012) TrakEM2 software for neural circuit reconstruction. PLoS One 7:e38011.

Saalfeld S, Fetter R, Cardona A, Tomancak P (2012) Elastic volume reconstruction from series of ultra-thin microscopy

26

740   sections. Nat Methods 9:717–720.

741   **Schindelin J,** et al. (2012) Fiji: An open-source platform for biological-image analysis. Nat Methods 9:676–682.

742   **Fiala JC,** Harris KM (2001) Cylindrical diameters method for calibrating section thickness in serial electron microscopy. J
743   Microsc 202:468–472.

744   **Bourne JN,** Harris KM (2011) Coordination of size and number of excitatory and inhibitory synapses results in a balanced
745   structural plasticity along mature hippocampal CA1 dendrites during LTP. Hippocampus 21:354–373.

746   **Fiala JC,** et al. (2003) Timing of neuronal and glial ultrastructure disruption during brain slice preparation and recovery in
747   vitro. J Comp Neurol 465:90–103.

748   **Bowden JB,** Mendenhall JM, Abraham WC, Harris KM (2008) Microtubule number as a correlate of dendritic spine density
749   in dentate granule cells. Soc Neurosci Abstr 34: 636.20. 54.

750   **Fiala JC,** Harris KM (2001) Extending unbiased stereology of brain ultrastructure to three-dimensional volumes. J Am Med
751   Inform Assoc 8:1–16.

752   **Edwards J,** et al. (2014) VolRoverN: Enhancing surface and volumetric reconstruction for realistic dynamical simulation of
753   cellular and subcellular function. Neuroinformatics 12: 277–289.

754

755   **Jung JH**, Kirk LM, Bourne JN, Harris KM. Shortened tethering filaments stabilize presynaptic vesicles in support of elevated
756   release probability during LTP in rat hippocampus. Proceedings of the National Academy of Sciences. 2021; 118(17).

757   **Kasai H**, Ziv NE, Okazaki H, Yagishita S, Toyoizumi T. Spine dynamics in the brain, mental disorders and artificial neural
758   networks. Nature Reviews Neuroscience. 2021; 22(7):407–422.

759   **Motta A**, Berning M, Boergens KM, Staffler B, Beining M, Loomba S, Hennig P, Wissler H, Helmstaedter M. Dense
760   connectomic reconstruction in layer 4 of the somatosensory cortex. Science. 2019; 366(6469).

761   **Schultz SR**. Signal-to-noise ratio in neuroscience. Scholarpedia. 2007; 2(6):2046.

762   **Harvey, C.D.** and Svoboda, K., 2007. Locally dynamic synaptic learning rules in pyramidal neuron dendrites. *Nature*,
763   *450*(7173), pp.1195-1200.

764   **Yang, Y.** and Liu, J.J., 2022. Structural LTP: Signal transduction, actin cytoskeleton reorganization, and membrane
765   remodeling of dendritic spines. *Current Opinion in Neurobiology*, *74*, p.102534.

766   **Saxe, M.D.,** Battaglia, F., Wang, J.W., Malleret, G., David, D.J., Monckton, J.E., Garcia, A.D.R., Sofroniew, M.V., Kandel,
767   E.R., Santarelli, L. and Hen, R., 2006. Ablation of hippocampal neurogenesis impairs contextual fear conditioning and
768   synaptic plasticity in the dentate gyrus. *Proceedings of the National Academy of Sciences*, *103*(46), pp.17501-17506.

769   **Snyder, J.S.,** Kee, N. and Wojtowicz, J.M., 2001. Effects of adult neurogenesis on synaptic plasticity in the rat dentate
770   gyrus. *Journal of neurophysiology*, *85*(6), pp.2423-2431.

771   **Lopez-Rojas, J.,** Heine, M. and Kreutz, M.R., 2016. Plasticity of intrinsic excitability in mature granule cells of the dentate
772   gyrus. *Scientific reports*, *6*(1), pp.1-12.

773   **Krueppel, R.,** Remy, S. and Beck, H., 2011. Dendritic integration in hippocampal dentate granule cells. *Neuron*, *71*(3),
774   pp.512-528.

775   **Harris, K.M.,** 2020. Structural LTP: from synaptogenesis to regulated synapse enlargement and clustering. *Current opinion
776   in neurobiology*, *63*, pp.189-197.

777   **Kuwajima, M.,** Mendenhall, J.M., Lindsey, L.F. and Harris, K.M., 2013. Automated transmission-mode scanning electron
778   microscopy (tSEM) for large volume analysis at nanoscale resolution. *PLoS One*, *8*(3), p.e59573.

779   **Harris, K.M.,** Hubbard, D.D., Kuwajima, M., Abraham, W.C., Bourne, J.N., Bowden, J.B., Haessly, A., Mendenhall, J.M.,

780 Parker, P.H., Shi, B. and Spacek, J., 2022. Dendritic Spine Density Scales with Microtubule Number in Rat Hippocampal
781 Dendrites. *Neuroscience*, *489*, pp.84-97.

782 **Harris, K.M.**, Spacek, J., Bell, M.E., Parker, P.H., Lindsey, L.F., Baden, A.D., Vogelstein, J.T. and Burns, R., 2015. A
783 resource from 3D electron microscopy of hippocampal neuropil for user training and tool development. *Scientific data*, *2*(1),
784 pp.1-19.

785 **Efron, B.** and Hastie, T., 2021. *Computer Age Statistical Inference, Student Edition: Algorithms, Evidence, and Data*
786 *Science* (Vol. 6). Cambridge University Press.
787

788

Table 3: Per animal analysis of SSC

| Time points	30 min				2 hours			
Animal #	Animal 1		Animal 2		Animal 3		Animal 4	
Weight (gr)	623		448		648		490	
age (postnatal day)	179		121		170		150	
time of delta-burst stimulation	10:30 am		10:30 am		09:30 am		09:30 am	
circadian cycle at delta-burst stimulation	dark		dark		dark		dark	
animal ID	LED50		LED56		LE108		LE113	
Condition	control	LTP	control	LTP	control	LTP	control	LTP
Series code	CLZBJ	TNKPS	NDKZB	MFBCF	JHHZS	HLWLQ	KSGRS	BBCHZ
mean fEPSP 5 min pre-delta-burst stimulation %	-3.84	-3.81	3.16	2.81	-2.36	0.04	0.65	-2.53
mean fEPSP last 5 min %	-5.38	33.61	5.28	48.33	-4.76	40.68	-1.10	34.45
# SDSA pairs	6	4	4	4	10	4	8	6
SDSA Scale factor	30	7	8	29	26	7	12	107
SDSA Median CV	0.65	0.31	0.71	0.76	0.44	0.42	0.63	0.38
# spine head volumes	130	110	79	78	112	111	127	115
spine head volume Scale factor	57	147	64	158	49	110	110	141
# Clusters for spine head volumes	5	11	4	5	6	8	5	9
Entropy	1.97	3.1	1.77	1.93	2.16	2.68	1.92	2.89
KL divergence	0.35	0.36	0.23	0.40	0.43	0.32	0.41	0.28
# Clusters (Bootstrapping)	4 ± 0.47	10 ± 0.55	4± 0.39	4 ± 0.5	6 ± 0.38	7 ± 0.71	5 ± 0.38	8± 0.6
Entropy (Bootstrapping)	1.92 ± 0.06	2.98 ± 0.1	1.7 ± 0.13	1.86 ± 0.1	2.1 ± 0.1	2.54 ± 0.1	1.86 ± 0.1	2.77 ± 0.1
KL divergence (Bootstrapping)	0.14 ± 0.12	0.31 ± 0.09	0.24 ± 0.12	0.27 ± 0.13	0.46 ± 0.1	0.27 ± 0.1	0.42 ± 0.12	0.31 ± 0.08

Table 3: For column with the term (± SE), SE stands for standard error calculated with bootstrapping using algorithm 1 and 2 , concurrently.

29
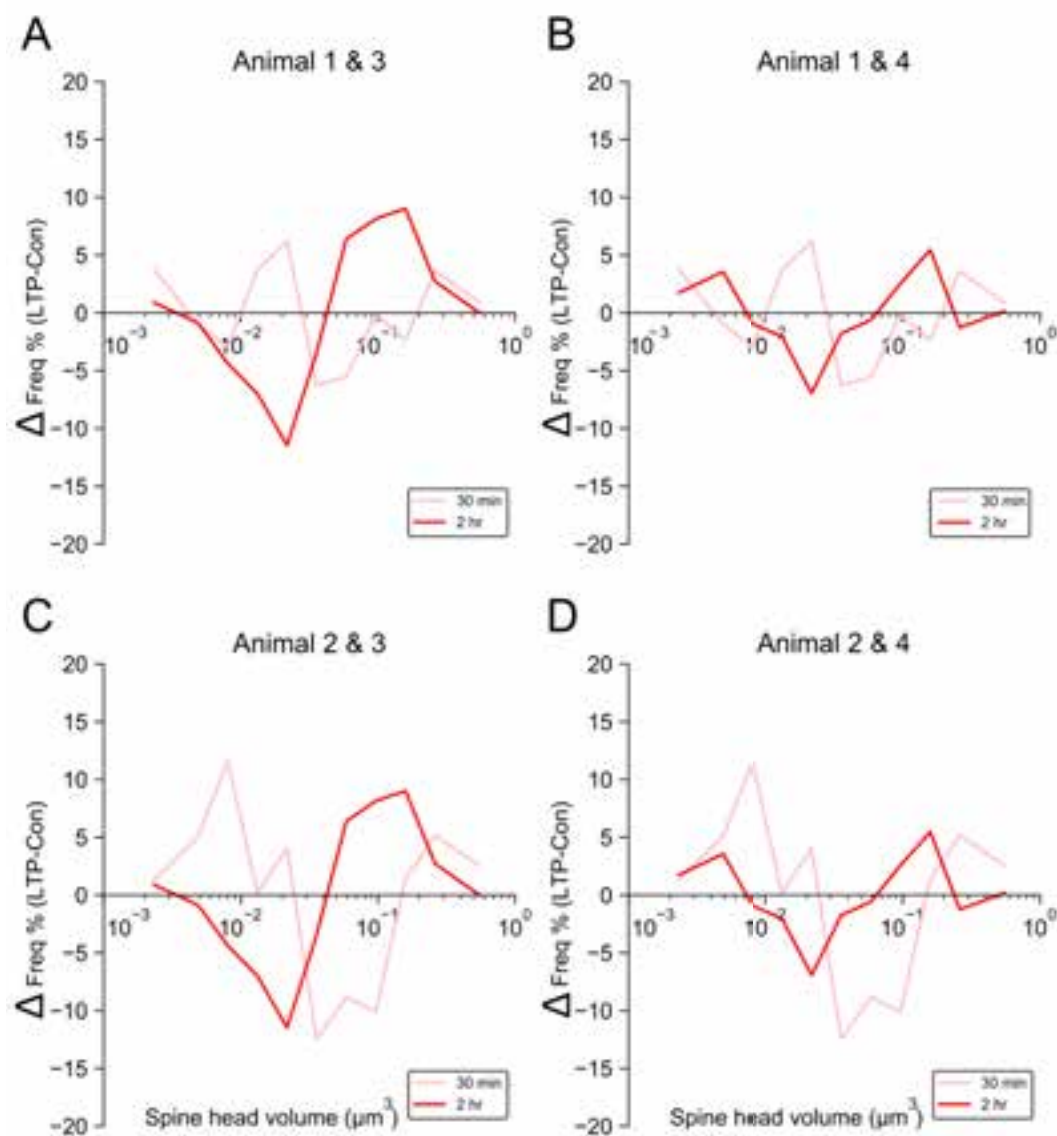
Supplementary Fig. 1

Change relative to control hemispheres in the distribution of spine head volumes at 30 min and 2 hr after the induction of LTP per animal. Difference between the frequency of spine head volumes in 30 min LTP and 2 hr LTP conditions. (A) Animal 1 & 3 (B) Animal 1 & 4 (C) Animal 2 & 3 (D) Animal 2 & 4.

30
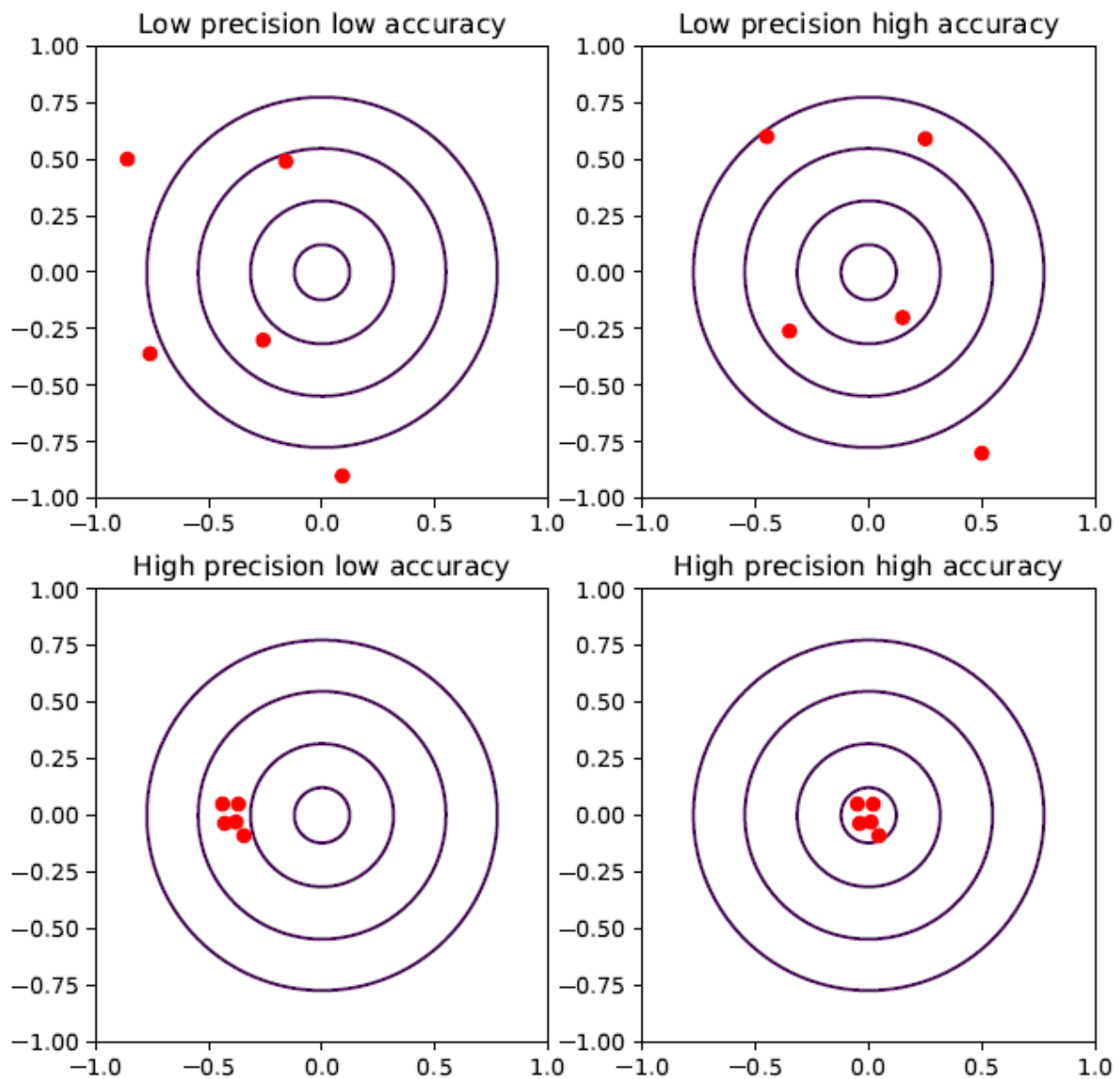
808 **Supplementary Fig. 2**

809 **Dart precision versus accuracy.** Precision concerns the degree of reproducibility of a process. When a process or system

810 is repeated with the same input the amount of variation in the output shows the precision level of the process. For accuracy

811 there is a reference frame with which the average value of measurements is compared. The graphs illustrate a low precision

812 and low accuracy outcome (top left), low precision and high accuracy (top right; the average of the positions is almost on

813 the bull's eye), high precision and low accuracy (bottom left), and high precision and high accuracy (bottom right).

814
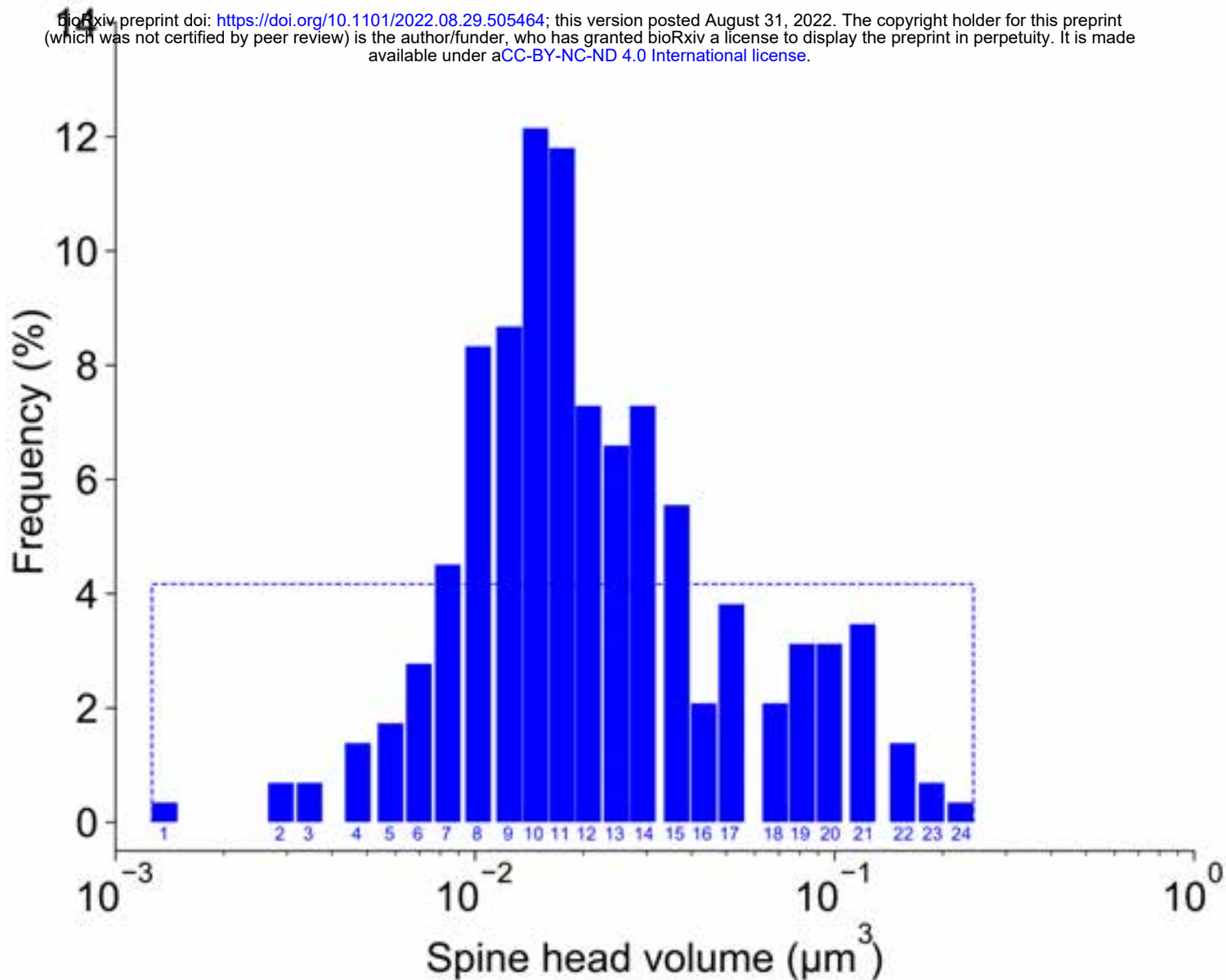
Supplementary Fig. 3

CA1 24 distinguishable clusters. The Y axis indicates the frequency of spine head volumes within each cluster and the X axis indicates the spine head volumes values in the log scale. The dash rectangular box around the histogram is the frequency of spine head volumes if the 288 spine head volumes were distributed uniformly among the 24 clusters.

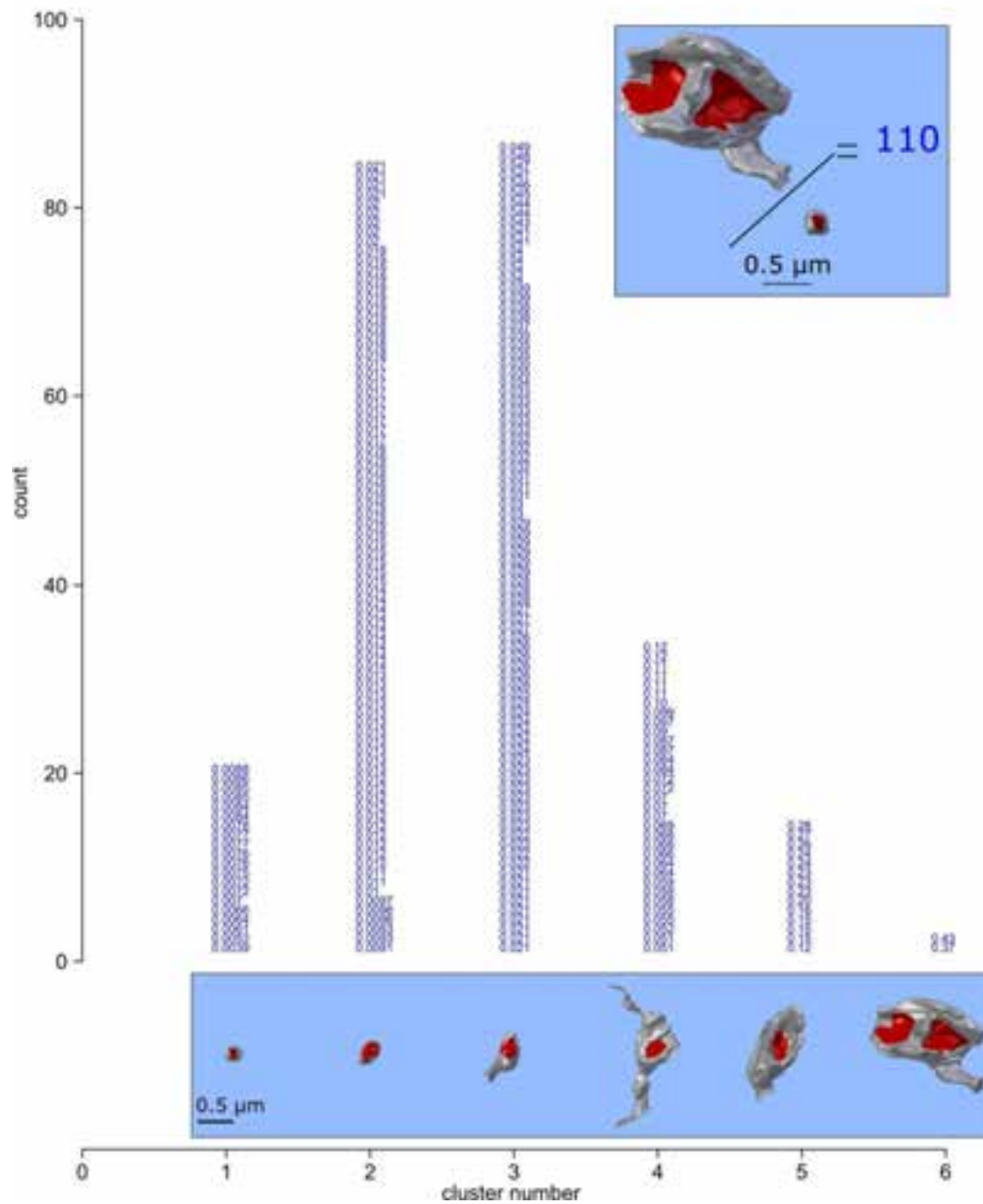Histogram of Spine Head Volume Categories (DG 30 min Control)

823
824
825
826
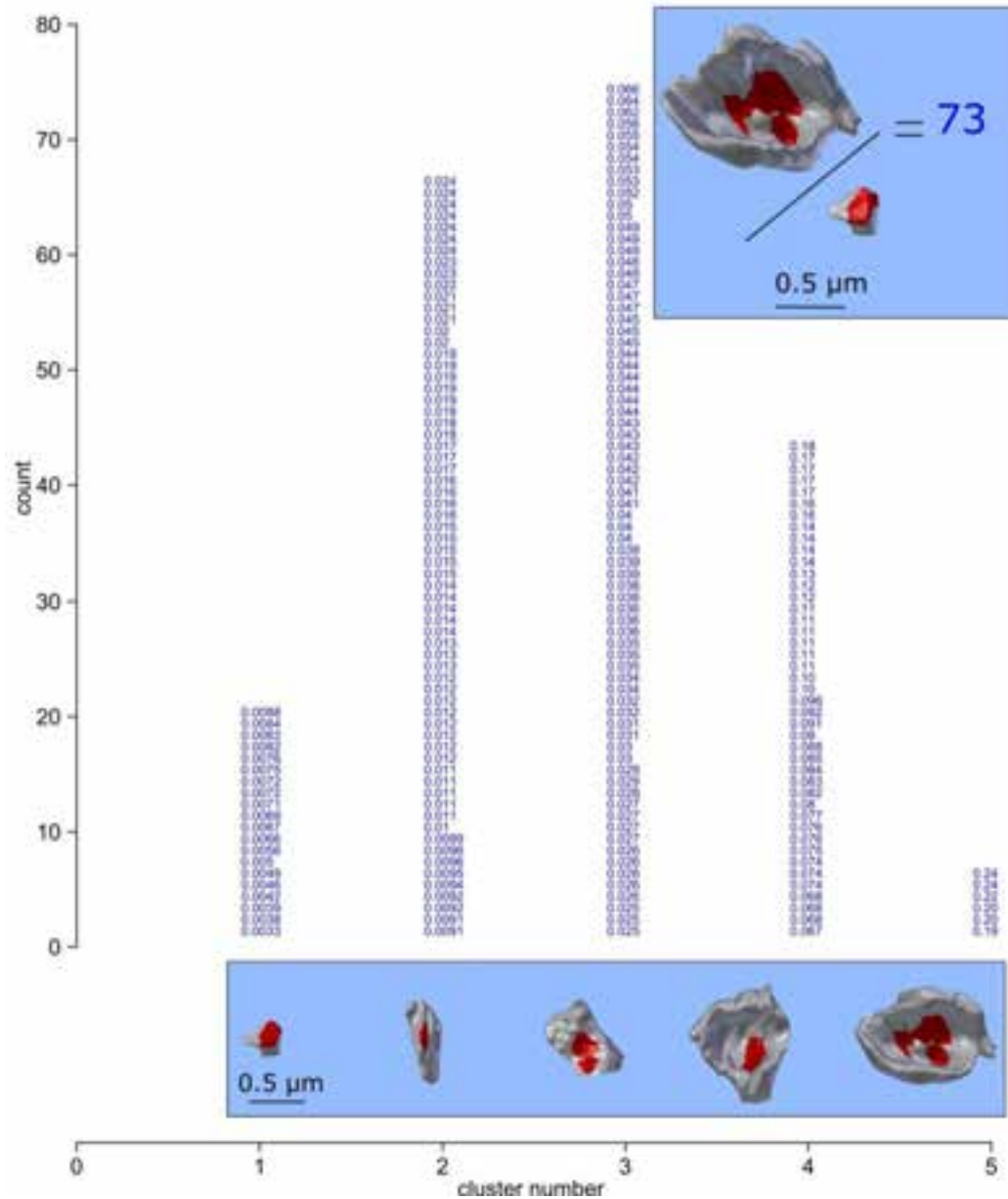
Supplementary Fig. 4

The clustering of 209 spine head volumes of two rats (concatenated data) both in control conditions. (30 min control data) To analyze synapses in the whole reconstructed cube, the 209 spine head volumes are clustered into 5 distinguishable categories using algorithm 2 based on the median value CV calculated from 10 SDSA pairs detected in the reconstructed cube. Median value of 10 CVs calculated from analysis illustrated in **Fig. 3**A with the value of 0.65. The Y axis shows the number of spine head volumes within each category. The 3D object below each category (vertical column) is the actual 3D reconstructed spine head volume of the largest head volume in the category. The X axis shows the distinguishable categories number.

835
836
837
838
839

840 **Supplementary Fig. 5**

841 **The clustering of 188 spine head volumes of two rats (concatenated data) both in LTP conditions. (30 min LTP**
842 **data)**

Histogram of Spine Head Volume Categories (DG 2hr Control)

843

Supplementary Fig. 6

The clustering of 239 spine head volumes of two rats (concatenated data) both in control conditions. (2 hr control data)

847
848
849

850 **Supplementary Fig. 7**

851 **The clustering of 226 spine head volumes of two rats (concatenated data) both in LTP conditions. (2 hr LTP data)**